*2*

# Synthesis and Characterization of Nanoporous Carbon and Its Electrochemical Application to Electrode Material for Supercapacitors

Gyoung-Ja Lee and Su-Il Pyun*

*Department of Materials Science and Engineering, Korea Advanced Institute of Science and Technology, Guseong-dong, Yuseong-gu, Daejeon, Republic of Korea*
**Corresponding author*

## I. INTRODUCTION

Nanoporous carbons have played a key role in many areas of modern science and technology such as purification of liquids and gases,[1,2] separation of mixture,[3,4] catalyst for reaction,[5-7] and storage of energy[8-17]. Especially, the highly porous carbons are widely used as electrode materials in electric double-layer capacitors (EDLCs), due to such advantageous features as high surface area, good electrical conductivity, and adequate corrosion resistance.[8-17] The pores are classified into three groups according to their size:

- pores with width (distance between the walls of a slit-shaped pore) smaller than 2 nm are called micropores,
- pores with width between 2 nm and 50 nm are called mesopores, and
- pores with width larger than 50 nm are called macropores.

*Modern Aspects of Electrochemistry*, Number 41, edited by C, Vayenas et al., Springer, New York, 2007.

The physical and chemical activation processes have been generally employed to prepare the porous carbons.[18-35] However, the pore structures are not easily controlled by the activation processes and the size of the pores generated by the activation processes is limited to the micropore range only. Recently, much attention has been paid to the synthesis of meso/macroporous carbons with various pore structures and pore size distributions (PSD) by using various types of such inorganic templates as silica materials and zeolites.[17,36-55]

The electro-active surface of the porous carbon electrode for EDLCs is accessible only through the cumulative resistance of the electrolyte inside the pore. Therefore, the porous structure of the porous carbon becomes one of the most important factors influencing the energy/power densities. Fractal analysis has proven to be useful to describe the geometric and structural properties of rough surfaces and pore surfaces.[56-66]

There are two conventional definitions in describing the fractality of porous material - the pore fractal dimension which represents the pore distribution irregularity[56,59,62] and the surface fractal dimension which characterizes the pore surface irregularity.[56,58,65] Since the geometry and structure of the pore surfaces are closely related to the electro-active surface area which plays a key role in the increases of capacity and rate capability in practical viewpoint, the microstructures of the pores have been quantitatively characterized by many researchers based upon the fractal theory.

In this respect, this review provides a comprehensive survey of synthetic methods and physicochemical properties of the porous carbon materials. Furthermore, as electrochemical applications of the porous carbons to electrode materials for supercapacitor, the effects of geometric heterogeneity and surface inhomogeneity on ion penetration into the pores during double-layer charging/ discharging are discussed in detail by using ac-impedance spectroscopy, current transient technique, and cyclic voltammetry.

The structure of this review is as follows: in Section II, the activation and templating methods for preparing the porous carbons are briefly summarized. Section III surveys the structural characteristics of the porous carbons by using gas adsorption method. In Section IV, the molecular probe method and the image analysis method for quantitative characterization of the pore surface irregularity and the size distribution irregularity based upon the fractal theory are discussed in detail. Section V is devoted to

the investigation of the electrochemical performance of the porous carbon electrodes for EDLCs considering the effects of geometric heterogeneity and surface inhomogeneity on kinetics of double-layer charging/discharging.

## II. PREPARATION OF POROUS CARBONS

### 1. Activation method

The activated carbons have been prepared by carbonization of precursors, i.e., raw materials with subsequent activation by physical treatment and/or chemical treatment. The activation procedure is conducted in order to enlarge the volume and size of the pores which were already created during the carbonization process and to create some new porosity. Most commonly employed activation methods are divided into physical and chemical activations.[14-16,18-35]

In physical activation, the gasification of the carbonized carbon usually occurs at higher temperature above 800 $^{o}$C in the presence of suitable oxidizing gases such as steam, carbon dioxide $CO_2$, or a mixture of these.[14-16,18,19,21-28,30,32,34,35] Activation of the carbon in atmospheres of steam and $CO_2$ occurs by the following endothermic reactions.

$$C\,(s) + H_2O\,(g) \rightarrow CO\,(g) + H_2\,(g) \quad (1)$$

$$C\,(s) + CO_2\,(g) \rightarrow 2CO\,(g) \quad (2)$$

Walker et al.[18] found that the reaction (2) took place uniformly throughout the entire volume of the carbons during gasification, resulting in the attainment of high internal surface area. Since the reactions of the carbon with steam and $CO_2$ are both endothermic, the external heating is required to drive the above reactions and to maintain the reaction temperature. The activation with $CO_2$ involves a less energetic reaction than that with steam and thus requires a higher temperature.

The surface area, the pore size, and the carbon yield are greatly influenced by oxidizing gas, heat-treatment temperature, and activation time. In addition, the oxidative activation introduced the surface acidic functional groups (SAFGs) on the pore surfaces of the carbon. The amounts of the SAFGs can be also controlled by

changing the activation conditions. Extensive burn-off at higher temperatures increases the surface area and pore size with less development of the SAFGs.

In chemical activation, the carbonaceous precursor is impregnated with a chemical agent, and then the impregnated product is pyrolyzed between 400 $^{o}$C and 800 $^{o}$C in an inert atmosphere. After that, the pyrolyzed product is cooled and washed exhaustively in order to remove the chemical agent, followed by filtration of the carbon materials.[19-23,26,29,31-35] The chemical agents used are normally alkali, alkali earth metal, and some acids such as KOH,[22,26,29,32,34,35] $K_2CO_3$,[32] NaOH,[32,34] $Na_2CO_3$,[32] $ZnCl_2$,[20-23] and $H_3PO_4$,[23,31,33] etc.

The main advantages of the chemical activation compared to the physical activation are lower activation temperature, shorter activation time, and higher development of the porosity. Furthermore, since the chemical agents used are just substances with dehydrogenation properties which inhibit formation of tar and reduce the production of other volatile products, the carbon yields of the chemically-activated carbons are usually higher than those of the physically-activated carbons. However, the general mechanism of the chemical activation is not well understood, as compared to that of the physical activation. Other disadvantages of the chemical activation are the need of additional washing procedure in order to remove the chemical agents and the corrosiveness of the chemical activation process.

Since the heat-treatment temperature used in the chemical activation is lower than that used in the physical activation, the porous structure is more developed in the case of the chemical activation. The higher the degree of impregnation, the larger is the pore size of the activated carbon. Generally, kind of chemical agent, impregnation ratio of chemical agent to the carbonaceous material, and physical mixing method for distribution of chemical agent into the carbonaceous material largely affect the resulting pore structures of the chemically-activated carbons.

The physical and chemical activation methods are effective in preparing the microporous carbons with high surface area. However, the pore structures of the carbons are not easily controlled by the activation processes and the size of the pores generated by the activation processes is limited to the micropore range only. Under these circumstances, the templating method which will be considered in the following Section II.2 has recently

attracted considerable attention in preparing porous carbons with various pore structures.

## 2. Templating Method

The meso/macroporous carbons have attracted much attention in their application as electrode materials in EDLCs, since the meso/macropores promote the formation of an effective double-layer or the transfer of ions into the pores, resulting in the increases in the electrolyte wettability and the rate capability.[67,68] In this regard, there has been considerable research targeted towards developing the synthetic methods of novel meso/macroporous carbons.[17,36-55,69-72] Various types of such inorganic templates as silica materials and zeolites are widely used for the synthesis of the meso/macroporous carbons, since it was revealed[17,36-55] that these inorganic templates contribute to the formation of the meso/macropores with various pore structures and broad PSD.

In templating method, many polymeric precursors including resorcinol-formaldehyde gel,[38,40,42,69,70,73-76] furfuryl alcohol,[41,49,53,55,76,77] phenolic resin,[49,72,74] melamine-formaldehyde resin,[69,72] and mesophase pitch,[17,45,46,54] etc. are generally used as carbonaceous precursors. The porous carbons are prepared by templating method according to the following procedures:

1. mixing of inorganic templates and carbonaceous precursors,
2. polymerization of the initial mixture,
3. carbonization of the polymerized composite, and
4. removal of the inorganic template.

Among the inorganic templates, zeolite produces more regulated pores as compared to the silica template. If nano-channels in zeolite are completely filled with carbonaceous precursor and then the carbon materials are extracted from the zeolite framework, one can obtain the porous carbon of which structure reflects the porosity of the original zeolite template. The ordered mesoporous silica templates, e.g., MCM-48[38,39,47] and SBA-15[47] have been employed to prepare the ordered porous carbons by the procedures involving the pore filling of the silica template with carbonaceous precursor followed by carbonization and silica dissolution. The resulting pore sizes of the ordered mesoporous carbons are smaller than about 10 nm.

In order to prepare the meso/macropores with the size of several decades of nanometers, the silica colloids have been frequently used as a template since the colloidal silica templates are reproducible and effective for the synthesis of the porous carbons with larger pore size, broad PSD, high pore volume, and high surface area by sol-gel process.[17,38,40,42,45,46,54,55] The silica gels are produced from the polycondensation of tetramethoxy silane (TMOS) or tetraethoxy silane (TEOS) in the presence of an acid or base. The shape and size of the silica are significantly influenced by the degree of silica particle agglomeration which is dependent upon the sol-gel reaction conditions, and hence the pore structure which reflects the structure of the silica template also depends upon the sol-gel reaction conditions, e.g., pH, amount of the silica template, and gelation temperature.

Recently, Pyun et al.[17,54,55] prepared various meso/ macroporous carbon specimens with various pore structures using the templating method with the changes of carbonaceous precursor, colloidal silica sol solution, amount of the silica template, and pH. Figure 1 plots the PSD curves for three kinds of mesoporous carbon specimens I, II, and III synthesized by using furfuryl alcohol, $C_5H_6O_2$ and commercial colloidal silica sol solution of Ludox SM-30 as a carbonaceous precursor and silica template, respectively, with the change of pH value of initial solution mixture.[55] The mixture of furfuryl alcohol and silica sol solution was heated in a vacuum oven at 100 °C for 5 days to polymerize the furfuryl alcohol. After that, the composite was carbonized at 900 °C for 3 h under Ar gas atmosphere, followed by dissolution of silica with 48 wt. % aqueous HF solution at room temperature.

It is noticeable from Figure 1 and Table 1 that the values of average pore diameter $D_{ave}$ and standard deviation of PSD $\sigma$ for specimens I, II, and III increased as well with increasing pH. Since the silica particles in colloidal silica sol solution of Ludox SM-30 have a uniform particle size of about 7 nm, it is reasonable to say that the formation of the pores larger than silica particle size is caused by the agglomeration of the silica sol particles. Besides, as the pH increased, the values of micro- and mesoporosity decreased, whereas that value of macroporosity increased. Accordingly, it is suggested that as the pH increases, the stability of silica particles decreases and hence causes higher agglomeration of the silica particles, which results in the increase of the relative volume fraction of the pores with a larger size.

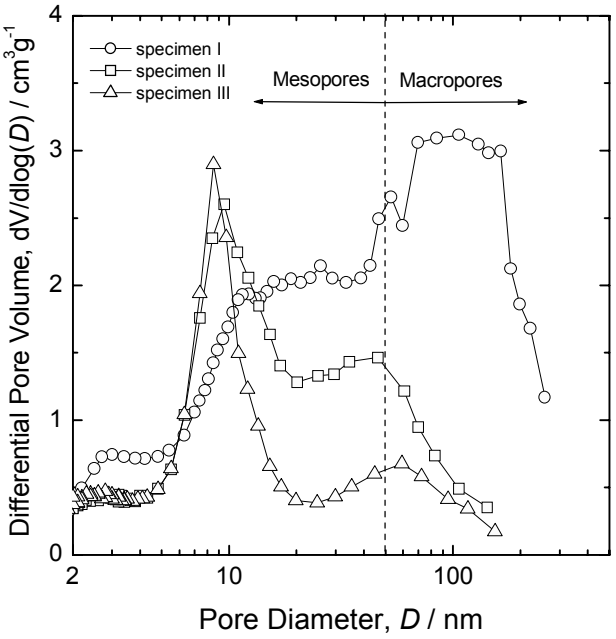



Figure 1. Plots of differential pore volume against pore diameter calculated from the $N_2$ gas adsorption isotherms obtained from meso/macroporous carbon specimens I (-○-), II (-□-), and III (-Δ-) using Barrett-Joyner-Halenda (BJH) method. Reprinted with permission from G. -J. Lee and S. -I. Pyun, *Carbon*, **43** (2005) 1804. Copyright © 2005, with permission from Elsevier.

## III. STRUCTURAL CHARACTERISTICS OF POROUS CARBONS

### 1. Types of Adsorption Isotherms and Hysteresis Loops

The first systematic attempt to interpret adsorption isotherms for gas/solid equilibria was by Braunauer, Deming, Deming, and Teller (BDDT) in 1940.[78] They classified the adsorption isotherms into five types, and the BDDT classification became the core of the modern International Union of Pure and Applied Chemistry

**Table 1.**
**The Pore Structures and Surface Fractal Characteristics of Meso/Macroporous Carbon Specimens I, II, and III Calculated from the Analyses of the $N_2$ Gas Adsorption Isotherms. Reprinted with permission from G. -J. Lee and S. -I. Pyun, *Carbon*, 43 (2005) 1804. Copyright © 2005, with permission from Elsevier.**

| Specimen | BET surface area, $A_{BET}$ ($m^2\ g^{-1}$) | Micro-porosity[a] | Meso-porosity[a] | Macro-porosity[a] | Average pore diameter, $D_{ave}$ (nm) | Standard deviation of PSD, σ (nm) | Pore radius of the maximum differential pore volume, $r_{max}$ (nm) | Surface fractal dimension, $d_{surf,SP}$[a] | Low-end thickness, $t_{ad,min}$ (nm) | High-end thickness, $t_{ad,max}$ (nm) |
|---|---|---|---|---|---|---|---|---|---|---|
| I ($SiO_2/C_5H_6O_2$ = 0.7, pH = 10.2) | 849 | 0.01 | 0.49 | 0.50 | 17.0 | 74.2 | 53.4 | 2.51 ± 0.03 | 0.35 | 36.74 |
| II ($SiO_2/C_5H_6O_2$ = 0.7, pH = 8.7) | 826 | 0.04 | 0.75 | 0.21 | 8.8 | 23.2 | 4.8 | 2.62 ± 0.02 | 0.35 | 3.68 |
| III ($SiO_2/C_5H_6O_2$ = 0.7, pH = 7.2) | 790 | 0.06 | 0.80 | 0.14 | 6.4 | 20.9 | 4.3 | 2.66 ± 0.02 | 0.35 | 3.00 |

[a]Dimensionless

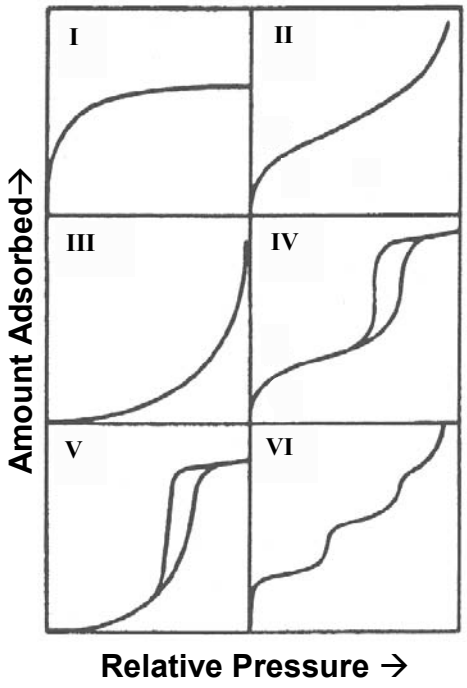



Figure 2. Classification of adsorption/desorption isotherms.

(IUPAC) classification of the adsorption isotherms[79] in Figure 2. The sixth isotherm in Figure 2 is recently added.

Type I isotherms are originally known as Langmuir isotherms since they represent Langmuir mechanism of monolayer coverage. In fact, most Type I isotherms can be attributed to the physisorption on the microporous adsorbents with relatively small external surfaces.Type II isotherms (S-shaped or sigmoid) are monolayer-multilayer isotherms, which are normally obtained from non-porous or macroporous adsorbents. Type IV isotherms are given by adsorbents which possess mesopore structure, such as many silica gels, mesoporous carbons, and other porous oxides. The remaining isotherms in the IUPAC classification exhibit particular features, which indicate weak adsorbate-adsorbent interactions in the case of Type III and V isotherms. The stepwise Type VI isotherms, indicative of a nonporous solid with an almost completely uniform surface, are quite rare.

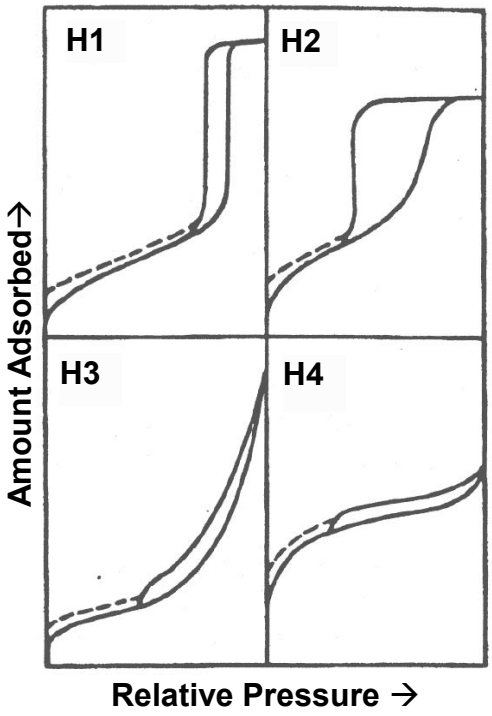



Figure 3. Classification of adsorption/desorption hysteresis loops.

For many of activated microporous carbons,[80-84] the isotherms exhibit prominent adsorption at low relative pressures and then level off, i.e., the isotherms exhibit Type I behavior. Type I isotherms may be also observed in the mesoporous materials with pore sizes close to the micropore range. In particular, in the case of gas adsorption on highly uniform cylindrical pores, the adsorption isotherms exhibit discernible steps at relative pressures down to 0.1 or perhaps even lower.[85-87] Such Type I behavior can be indicative of some degree of broadening of the mesopore size distribution.

Adsorption on macroporous carbons proceeds via multilayer formation in such a manner that the amount adsorbed increases gradually as the relative pressure increases, and then the multilayer build-up near the saturation vapor pressure may be abrupt. This unrestricted monolayer-multilayer adsorption gives rise to Type II and III isotherms. In this case, the adsorption and desorption

branches of the isotherms coincide fairly well with each other, i.e., there is no hysteresis loop.

On the other hand, for the mesoporous carbons, the gas adsorption process changes with increasing relative pressure as follows: first monolayer-multilayer adsorption on the pore surfaces, then capillary condensation in the mesopores, and finally multilayer adsorption on the outer surfaces in sequence (Types IV and V isotherms). Therefore, the adsorption process for the mesoporous carbons is initially similar to that for the macroporous carbons, but at higher relative pressures the amount adsorbed rises very steeply due to the capillary condensation in the mesopores.

Capillary condensation and evaporation do not reversibly take place at the same pressure, which leads to the appearance of hysteresis loops. The hysteresis loop, which is due to the different processes between adsorption into and desorption from the mesopores, is closely related to the pore structure of the mesoporous material.[54,86,88] Thus, the pore structures of the mesoporous carbons can be estimated from the shape of the hysteresis loop.

According to the IUPAC,[79] the hysteresis loops are classified into four types from Type H1 to Type H4. The Type H1 loop in Figure 3 is characteristic of the mesoporous materials consisting of the pores with cylindrical pore geometry or the pores with high degree of pore size uniformity.[88,89] Hence, the appearance of the H1 loop on the adsorption isotherms for the porous solids generally indicates facile pore connectivity and relative narrow PSD.

Many porous adsorbents give Type H2 hysteresis loop, but in such systems PSD or pore shape is not well-defined. Indeed, the H2 loop is especially difficult to interpret. In the past it was considered to be a result of the presence of the pores with narrow necks and wide bodies (ink-bottle pores), but it is now recognized that this provides an over-simplified picture and the pore connectivity effects must be taken into account.[79]

Type H3 hysteresis loop, which does not level off near the saturation vapor pressure, is characteristic of the mesoporous materials being comprised of agglomerates of plate-like particles with slit-shaped pores.[79,86] Type H4 loop, which features parallel and almost horizontal branches, is attributable to the adsorption/ desorption in narrow slit-like pores. However, Type H4 loop was recently reported for MCM-41 being comprised of particles with internal voids of irregular shape and broad PSD,[90] and also

observed for hollow spheres with walls composed of ordered mesoporous silica.[91]

## 2. Determinations of Surface Area and Pore Size Distribution

The Brunauer, Emmett, and Teller (BET) theory,[92] which generalized the Langmuir theory[93] by incorporating the concept of multilayer adsorption, has been generally used for the determination of the surface area of porous materials, in spite of oversimplication of the model upon which the theory is based. The derivation of the BET equation involves the following assumptions: The surface is flat; All adsorption sites exhibit the same adsorption energy; There are no lateral interactions between adsorbed molecules; The adsorption energy for all the molecules except for the first layer is equal to the liquefaction energy, and an infinite number of layers can be formed on the surface.

Assuming that the condensation rate of the gas molecules onto an already adsorbed layer is equal to the evaporation rate of the molecules from the adsorbed layer, the BET equation can be obtained in a linear form as follows

$$\frac{p}{V(p^{\circ}-p)} = \frac{1}{V_{\text{momo}}C} + \frac{C-1}{V_{\text{mono}}C}\left(\frac{p}{p^{\circ}}\right) \tag{3}$$

where $V$ is the volume of adsorbed gas molecules at the relative pressure $p/p^o$; $V_{\text{mono}}$, the volume of monolayer coverage; $p^o$, the saturation pressure of the gas, and $p$ represents the adsorption equilibrium pressure of the gas. The values of $V_{\text{mono}}$ and constant $C$ can be estimated from the linearity of the plot of $p/V(p^o - p)$ *vs.* $p/p^o$, i.e., the BET plot. According to the BET theory, the value of $C$ is related to the enthalpy (heat) of adsorption in the first adsorbed layer $Q_1$

$$C \propto \exp\left(\frac{Q_1 - Q_{\text{L}}}{RT}\right) \tag{4}$$

where $Q_L$ is the heat of liquefaction of the adsorbate, $R$ and $T$ are the gas constant and the absolute temperature, respectively. It is now recognized that the value of $C$ gives an indication of the magnitude of the adsorbent-adsorbate interaction energy.

The total BET surface area $A_{\mathrm{BET}}$ is calculated from the volume of monolayer coverage $V_{\mathrm{mono}}$ to

$$A_{\mathrm{BET}} = \frac{V_{\mathrm{mono}} A_{\mathrm{c}} N_{\mathrm{A}}}{V_{\mathrm{m}}} \tag{5}$$

where $A_{\mathrm{c}}$ is the molecular cross-sectional area; $N_A$, the Avogadro constant ($6.02 \times 10^{23}$ molecules $\mathrm{mol}^{-1}$), and $V_{\mathrm{m}}$ is the molar volume of the ideal gas (22414 $\mathrm{cm}^3$). The specific surface area can be obtained by dividing $A_{\mathrm{BET}}$ by the mass of the adsorbent $m$. The values of $A_{\mathrm{c}}$ are given as 0.162 $\mathrm{nm}^2$, 0.142 $\mathrm{nm}^2$, and 0.215 $\mathrm{nm}^2$ for $N_2$, Ar, and Kr, respectively.[94]

Now let us overview the theoretical adsorption models for characterization of the pore structures according to the pore size range. For physical adsorption of the gas molecules on such microporous solids as activated carbons and zeolites, Dubinin and Radushkevich[95] developed an empirical equation, which describes the volume filling process in the micropores. Their theory incorporates earlier work by Polanyi[96] in regard to the adsorption potential $A_{\mathrm{ad}}$ defined as

$$A_{\mathrm{ad}} = -\Delta G = RT \ln(p^{\mathrm{o}} / p) \tag{6}$$

Here, $\Delta G$ is Gibbs' free energy. For carbon materials being comprised of slit-shaped pores, the Dubinin-Radushkevich (D-R) equation is given as

$$V = V_{\mathrm{o}} \exp\left[ -\left( \frac{A_{\mathrm{ad}}}{\beta E_{\mathrm{o}}} \right)^2 \right] \tag{7}$$

where $V_{\mathrm{o}}$ is the total micropore volume; $\beta$, the affinity coefficient, and $E_o$ is the characteristic adsorption potential for the reference vapor, benzene. Dubinin and Stoeckli[97] suggested the relationship between $E_o$ and average half-width $x$ of the slit-shaped pores, $E_o = k/x$. Here, the empirical constant $k$ is assumed to be 12 kJ nm $\mathrm{mol}^{-1}$ for nitrogen gas.[94]

A more general expression, called the Dubinin-Astakhov (D-A) equation[98] is written as

$$V = V_o \exp\left[-\left(\frac{A_{ad}}{\beta E_o}\right)^n\right] \quad (8)$$

Here, $n$ is the equation parameter. The D-R equation is a special case for $n = 2$.

In order to determine the PSD of the micropores, Horvath-Kawazoe (H-K) method has been generally used. In 1983, Horvath and Kawazoe[99] developed a model for calculating the effective PSD of slit-shaped pores in molecular-sieve carbon from the adsorption isotherms. It is assumed that the micropores are either full or empty according to whether the adsorption pressure of the gas is greater or less than the characteristic value for particular micropore size. In H-K model, it is also assumed that the adsorbed phase thermodynamically behaves as a two-dimensional ideal gas.

The H-K method is based upon the model suggested by Everett and Powl[100] which describes the interaction potential of a single adsorbate molecule between two parallel planes of the atoms of graphitized carbon. In the H-K expansion of the Everett and Powl's work, the space between the parallel carbon planes, i.e., the pore is assumed to be filled with adsorbed gas molecules. Thus, the contribution of adsorbate-adsorbate-adsorbent interaction to the total interaction potential is considered along with that of adsorbate-adsorbent interaction.

The H-K method has been modified by many researchers in consideration of the pore geometry. Saito and Foley[101] extended the H-K approach to the case of cylindrical pores. Based upon the Everett-Powl model, they assumed that the pore is perfectly cylindrical in shape and infinite in length, and the inside wall of the cylindrical pore is a single layer of atoms with a continuum of interaction potential. Cheng and Yang[102] extended the H-K equation to the case of spherical pores, notably cavities in zeolite. In Cheng and Yang model, the only interactions are considered between the adsorbate and oxygen atoms of the spherical cavity wall within the zeolite, and the cavity wall is supposed to be comprised of a single lattice plane of atoms.

In the case of the meso/macropores, the physical adsorption related to the capillary condensation is generally described with the aid of following Kelvin equation[94,103]

$$\frac{1}{r_1}+\frac{1}{r_2}=-\frac{RT}{\gamma_L V_{cond}\cos\theta}\ln\left(\frac{p^*}{p^o}\right) \tag{9}$$

where $r_1$ and $r_2$ are two primary radius of curvature of the liquid meniscus in the pores; $\gamma_L$, the liquid surface tension; $V_{cond}$, the molar volume of the condensed adsorbate; $\theta$, the contact angle between the solid and condensed phase (taken to be zero for $N_2$, hence cos $\theta$ = 1), and $p^*$ represents the critical condensation pressure of the gas.

The pore shape is generally assumed to be either cylindrical or slit-shaped: in the former case, the meniscus is hemispherical, and hence $r_1$ is equal to $r_2$; in the latter case, the meniscus is hemicylindrical, and thus $r_1$ is equal to the width of the slit and $r_2$ is infinite. From the relation $\frac{1}{r_{L,m}}=\frac{1}{2}\left(\frac{1}{r_1}+\frac{1}{r_2}\right)$, the mean radius of curvature of the liquid meniscus, $r_{L,m}$ is expressed as

$$r_{L,m}=\frac{2\gamma_L V_{cond}\cos\theta}{RT\ln(p^*/p^o)} \tag{10}$$

It should be recognized that the Kelvin equation provides the core radius instead of the actual pore radius. The core radius represents the radius of the inner free space in the pore, which is not yet filled with the adsorbate. Therefore, in order to obtain the actual pore radius, the Kelvin equation needs to be corrected for the actual thickness of adsorbed molecule layers $t_{ad}$. The radius of a cylindrical pore, $r_p$ is given by

$$r_p = r_{L,m} + t_{ad} \tag{11}$$

and the width of a parallel-sided slit, $w_p$ is written as

$$w_p = r_{L,m} + 2t_{ad} \tag{12}$$

Based upon the Kelvin equation, the PSD of the meso/macropores has been generally determined by Barrett, Joyner, and Halenda (BJH) method.[104] Furthermore, the density functional theory[94] which is based upon a molecular-based statistical thermodynamic theory was recently introduced in order to analyze

the PSD of the porous materials from micropores to macropores in size in considerations of the adsorbate-adsorbate and adsorbate-adsorbent interaction energy parameters, the pore size, the pore geometry, and the temperature.

## IV. FRACTAL CHARACTERISTICS OF POROUS CARBONS

The real objects found in nature have complex structures which Euclidean geometry can not characterize. After Mandelbrot[105] developed a new geometry, i.e., fractal geometry, which provides a new paradigm for understanding many physical phenomena in nature, fractal geometry has been widely used in a number of fields, e.g., science, art,[106-108] economics,[109-112] etc. Especially, in science, fractal analysis has proven to be useful to describe the geometric and structural properties of rough surfaces and pore surfaces.[56-66] Since the geometry and structure of the pore surfaces are closely related to the electro-active surface area which plays a key role in the increases of capacity and rate capability in practical viewpoint, the microstructures of the pores have been quantitatively characterized by many researchers based upon the fractal theory.

There are two conventional definitions in describing the fractality of porous material—the surface fractal dimension[56,58,65] and the pore fractal dimension.[56,59,62] The former fractal dimension characterizes the pore surface irregularity: the larger the value of the surface fractal dimension is, the more irregular and the rougher is the pore surface. The surface fractal dimensions of 2 and 3 mean a perfectly flat pore surface and a very rough pore surface, respectively. On the other hand, the latter fractal dimension represents the pore distribution irregularity: the larger the value of the pore fractal dimension is, the narrower is the PSD that exhibits a power-law behavior. The pore fractal dimensions of 2 and 3 indicate the porous electrode with homogeneous PSD and that electrode composed of the almost same-sized pores, respectively.

Several simple relations have been proposed for the determination of the fractal dimensions from the results of such experiments as gas molecular probe method, transmission electron microscopy (TEM), small-angle X-ray scattering, neutron scattering, and laser light scattering.[63,66,113-116] Among those techniques, gas molecular probe method and image analysis method have been widely used for the calculation of the surface

and pore fractal dimensions of the porous materials, since theoretical bases are well established and their experimental procedures are relatively simple. The detailed descriptions of gas molecular probe method and image analysis method are given in the following Sections VI.1 and VI.2.

### 1. Molecular Probe Method Using Gas Adsorption

Since Avnir and Pfeifer's pioneer works[56,117-119] regarding the characterization of the surface irregularity at the molecular level by applying the fractal theory of surface science, molecular probe method using gas adsorption has played an important role in the determination of the surface fractal dimensions of the porous materials.

There are two molecular probe methods available for the determination of the surface fractal dimension. One is the multiprobe method (MP method),[56,117,120-133] which uses several kinds of multiprobe molecules with different molecular sizes. If the probe molecule is varied through a series of spheres with radius $r_m$, the surface fractal dimension is given by

$$N_{mono} \propto r_m^{-d_{surf,MP}} \tag{13}$$

Here, $N_{mono}$ is the number of adsorbed molecules to form a monolayer for each probe molecule and $d_{surf,MP}$ is the surface fractal dimension determined by using the MP method. The probe molecules need not to be spherical, provided they belong to a homologous series for which the ratio [linear extent $r_m$]$^2$ to molecular cross-sectional area $A_c$ is the same for all members, i.e., an isotropic series. In this case, Eq. (13) turns into

$$N_{mono} \propto A_c^{-\frac{d_{surf,MP}}{2}} \tag{14}$$

The MP method is widely applicable to various solid surfaces in whose system $N_{mono}$ can be accurately determined. It was recently reported[64,134-136] that even for the micropore whose pore width is greater than the bilayer thickness of $N_2$ (about 0.7 nm), $d_{surf,MP}$ can be determined using Eq. (14) if the monolayer evaluation fit for the micropore is introduced.

The other molecular probe method is the single-probe method (SP method), which is separately proposed by Pfeifer

et al.[56,58,60,137,138] In the SP method, a single adsorption isotherm is analyzed using a modified FHH theory. The FHH model first developed by Frenkel,[139] Halsey,[140] and Hill[141] describes a multilayer gas adsorption on the solid surface. Since the SP method is used only for one probe molecule, this method is more convenient than the MP method. However, there are many theoretical limitations in applying the SP method to determination of the surface fractal dimension. Therefore, it is really necessary to discuss about whether the SP method is an adequate tool or not before applying the SP method to certain system, in order to investigate the surface fractal dimension.

The theoretical assumptions used in the SP method are as follows:

1. The detailed structure of the layer of the adsorbed molecules is not important and is regarded as a liquid film.
2. The thickness of the layer of the adsorbed molecules is the characteristic distance scale for fractal surface.
3. Van der Waals attraction forces between solid/gas interactions and the liquid/gas surface tension forces are contributed to the grand potential of the system.

On the basis of the theory of Pfeifer et al.,[56,58,60,137,138] the surface fractal dimension can be determined from the gas adsorption isotherm according to the following equation

$$\ln\left(\frac{V}{V_{\text{mono}}}\right) = const. + C_{\text{SP}}\left[\ln\ln\left(\frac{p^{\text{o}}}{p}\right)\right] \tag{15}$$

where $C_{\text{SP}}$ is the power-law exponent which is dependent upon the surface fractal dimension determined by using the SP method $d_{\text{surf,SP}}$.

At the early stage of multilayer build-up, the interface is dominantly controlled by van der Waals forces between solid/gas interactions and the liquid/gas surface tension forces are neglected. Then, the relationship between $C_{\text{SP}}$ and $d_{\text{surf,SP}}$ is written as

$$C_{\text{SP}} = \left(\frac{d_{\text{surf,SP}} - 3}{3}\right) \tag{16}$$

For higher coverage, the interface is controlled by the liquid-gas surface tension forces (capillary condensation) and van der

Waals forces between solid/gas interactions are negligibly small. Then, the relationship between $C_{SP}$ and $d_{surf,SP}$ changes to the following expression.

$$C_{SP} = \left(d_{surf,SP} - 3\right) \tag{17}$$

Van der Waals forces between solid/gas interactions and the liquid/gas surface tension forces represent the limiting cases, but in general both the forces competitively affect the adsorption process. Therefore, in determining the surface fractal dimension by using the SP method, it is very important to use appropriate relation between $C_{SP}$ and $d_{surf,SP}$. According to Ismail and Pfeifer,[60] the threshold for the dominant forces between van der Waals forces and the liquid/gas surface tension forces is given as

$$\varepsilon = 3\left(1 + C_{SP}\right) - 2 \tag{18}$$

If $\varepsilon < 0$, the liquid/gas surface tension forces are dominant, while the van der Waals forces are dominant if $\varepsilon \geq 0$.

Pyun et al.[54,55,142] have investigated the surface fractal characteristics of the carbon specimens using the SP method. Figure 4 depicts the plots of ln $V/V_{mono}$ against lnln $(p^o/p)$ reconstructed from the nitrogen gas adsorption isotherms obtained from meso/macroporous carbon specimens (a) I, (b) II, and (c) III.[55] The values of $\varepsilon$ for specimens I, II, and III were determined to be –0.47, –0.14, and –0.02, respectively in the first linear segment, and thus the surface fractal dimensions $d_{surf,SP}$ were estimated from combined Eqs. (15) and (17). It is noticeable from Table 1 that the carbon specimen prepared at the higher pH value gave the lower value of $d_{surf,SP}$ than that specimen prepared at the lower pH value, which is due to more agglomeration of the silica sol particles. In their work, it is confirmed that as the silica-templated pores being comprised of the carbon specimen agglomerate, the irregularity of that pore surface decreases.

The number of adsorbed molecule layers $n_{ad}$ is calculated from the following relationship:[60]

$$n_{ad} = \frac{t_{ad}}{a_o} = \left(\frac{V}{V_{mono}}\right)^{1/\left(3-d_{surf,SP}\right)} \tag{19}$$

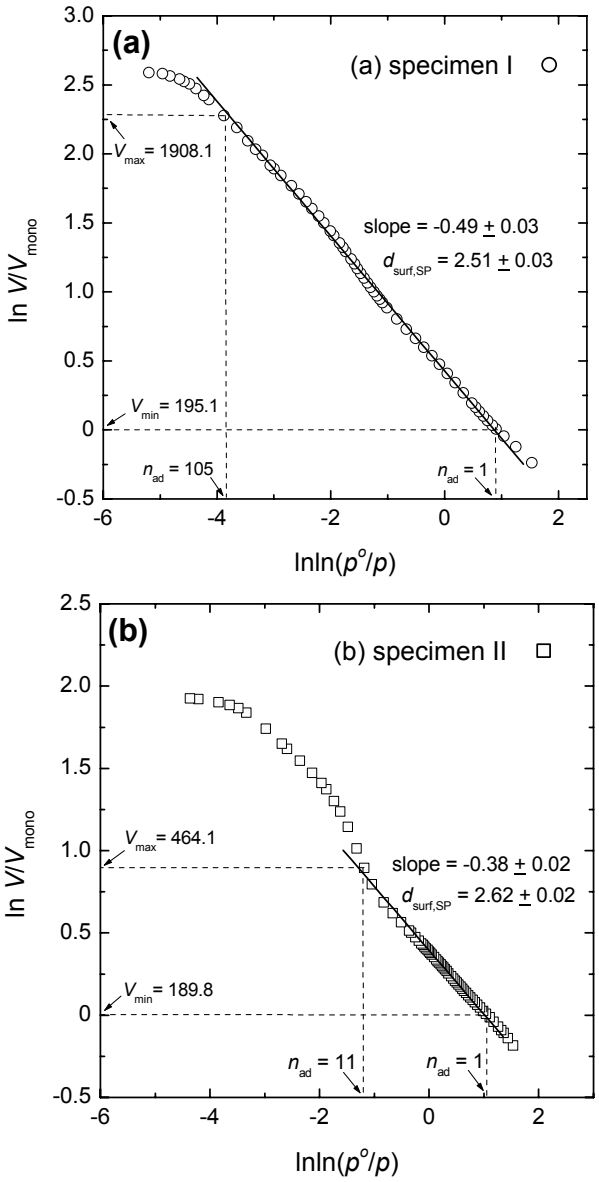



Figure 4. Plots of ln $V/V_{mono}$ against lnln ($p^o/p$) reconstructed from the $N_2$ gas adsorption isotherms obtained from the specimens (a) I (○), (b) II (□), and (c) III (Δ).Reprinted with permission from G. -J. Lee and S. -I. Pyun, *Carbon*, **43** (2005) 1804. Copyright © 2005, with permission from Elsevier.

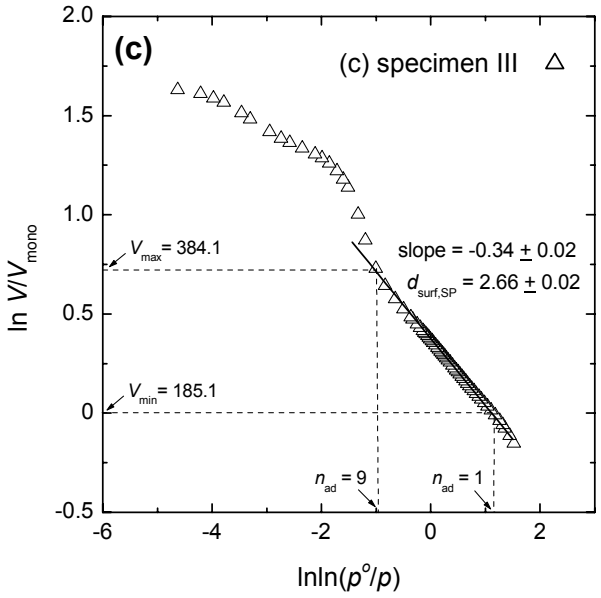



Figure 4. Continuation.

Here, the actual thickness of adsorbed molecule layers $t_{ad}$ is obtained by multiplying $n_{ad}$ by adsorbed molecule diameter $a_o$. The actual thickness range in which the fractal geometry is satisfied represents the length-scale cutoff range of fractality.[56,58] The value of the high-end thickness of the fractal regime $t_{ad,max}$ can be evaluated by using following equation

$$t_{ad,max} = t_{ad,min}\left(\frac{V_{max}}{V_{min}}\right)^{1/\left(3-d_{surf,SP}\right)} \tag{20}$$

where $t_{ad,max}$ is the value of the low-end thickness of the fractal regime, $V_{min}$ and $V_{max}$ are the lower and upper limits of the power-law regimes in the plot of ln $V$ against ln ln ($p^o/p$), respectively.

In Lee and Pyun's work,[55] it is interesting to note that $t_{ad,max}$ is slightly smaller in value than the pore radius of the maximum differential pore volume $r_{max}$ for specimens I, II, and III, as listed in

Table 1. As the relative pressure increases, the thickness of adsorbed molecule layers on the pore surfaces increases as well, and then the pore filling process caused by capillary condensation occurs first in the small pores simultaneously with the multilayer adsorption on the larger pores. For specimen III, the value of $t_{ad,max}$ is significantly larger than those values for the other specimens, which is ascribed to the fact that as a result of the pore filling process in the larger macropores the adsorbed volume starts to increase abruptly only near the saturation vapor pressure in the gas adsorption isotherm. From the above results, they suggested that $t_{ad,max}$ / $t_{ad,min}$ is closely related to $r_{max}$, that is, the larger $r_{max}$, the wider ranges the length-scale of the fractal regime in value.

It is reasonable to compare the length-scale range of the fractal regime each other for the carbon specimens based upon the value of $t_{ad,max}$. However, it is ambiguous that the value of $t_{ad,max}$ represents the actual outer cutoff length satisfying the fractal geometry or not. Since the gas molecule layers could more adsorb on the pore surface if the capillary condensation does not occur in the pores with maximum differential pore volume, the actual outer cutoff length could be larger in value than that of $t_{ad,max}$. Under these circumstances, for a better understanding of the outer cutoff of fractality, additional exact estimation of the outer cutoff length is still needed by using other complementary methods.

On the other hand, it is impossible to apply the SP method to the correct description of gas adsorption in the micropores, since the adsorption in the micropores does not occur by multilayer adsorption but by micropore volume filling process. In this case, the pore fractal dimension gives a physical importance for the description of structural heterogeneity of the microporous solids. Terzyk et al.[143-149] have intensively investigated the pore fractal characteristics of the microporous materials using gas adsorption isotherms theoretically simulated.

Based upon D-A equation[98] in consideration of PSD, the overall adsorption isotherm $\Theta$ of the microporous materials is written as

$$\Theta = \int_{x_{min}}^{x_{max}} \theta_L f_P(x) dx \tag{21}$$

The local adsorption isotherm $\theta_L$ is represented by the original D-A equation and $f_P(x)$ is the micropore size distribution ranging from $x_{min}$ to $x_{max}$ (the lower and upper limits of the slit-like

micropore half-width, respectively). If $f_P(x)$ is assumed to be PSD with pore fractality derived by Pfeifer and Avnir[56], $f_P(x)$ is given by

$$f_P(x) = \rho x^{2-d_{pore,SP}} \quad (x_{min} < x < x_{max}) \tag{22}$$

with

$$\rho = \frac{3 - d_{pore,SP}}{x_{max}^{3-d_{pore,SP}} - x_{min}^{3-d_{pore,SP}}} \tag{23}$$

where $d_{pore,SP}$ is the pore fractal dimension determined by using the SP method, $x_{min}$ and $x_{max}$ are the lower and upper limits of the pore fractality, respectively.

From the above, the overall adsorption isotherm $\Theta$ can be represented by[146]

$$\Theta = \int_{x_{min}}^{x_{max}} \exp(-\mu' A_{ad}^n x^n) \times \rho x^{2-d_{pore,SP}} dx \tag{24}$$

where $\mu' = (k\beta)^{-n}$ depends upon the adsorbate and the microporous structure ($\beta$ is the affinity coefficient and $k$ is an empirical constant assumed to be 12 kJ nm mol$^{-1}$ for nitrogen gas.[94])

Terzyk et al.[143] gave first the analytical solution of Eq. (24) as follows

$$\Theta = \frac{V}{V_o} = \frac{\rho}{n}(\mu' A_{ad}^n)^{(d_{pore,SP}-3)/n} \times \left[\gamma\left(\frac{3-d_{pore,SP}}{n}, x_{max}^n \mu' A_{ad}^n\right) - \gamma\left(\frac{3-d_{pore,SP}}{n}, x_{min}^n \mu' A_{ad}^n\right)\right] \tag{25}$$

where $\gamma$ is an incomplete gamma function. If $n = 2$, D-R isotherm is obtained in view of PSD with pore fractality.[150]

Recently, Lee and Pyun have focused on the characterization of pore fractality of the microporous carbon powder specimens by using nitrogen gas adsorption method based upon the D-A adsorption theory in consideration of PSD with pore fractality. Figure 5 envisages the nitrogen gas adsorption isotherm obtained from the as-reactivated carbon powder specimen prepared by reactivation of the commercially as-activated carbon powder at 1000 $^oC$ in an atmosphere of $CO_2$/CO gas mixture for 2 h. The solid

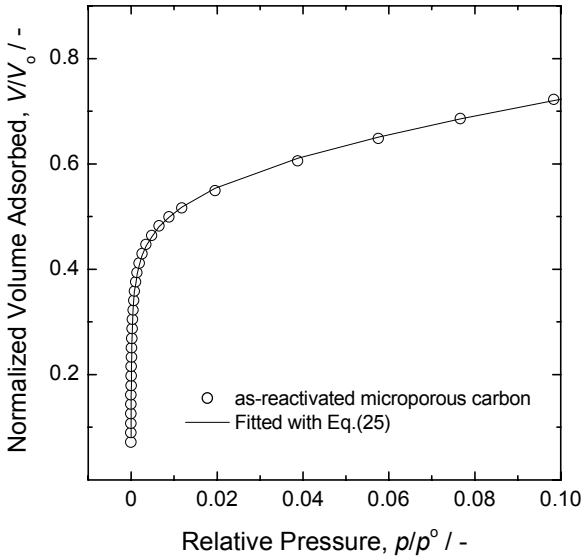



Figure 5. Nitrogen gas adsorption isotherm experimentally obtained from the as-reactivated carbon powder specimen prepared by reactivation of the commercially as-activated carbon powder at 1000 $^oC$ in an atmosphere of $CO_2$/CO gas mixture for 2 h. The solid lines were determined from the non-linear fitting of the experimental adsorption isotherms with Eq. (25).

line in Figure 5 was determined from the non-linear fitting of the experimental adsorption isotherm with Eq. (25). From the quantitative comparison of the adsorption isotherm experimentally obtained with that theoretically calculated, the values of $d_{pore,SP}$, $x_{min}$, and $x_{max}$ were estimated to be 2.523 $\pm$ 0.035, 0.26 nm, and 0.50 nm, respectively. This will be reported in greater detail in a future publication.

## 2. Image Analysis Method

The solid surfaces and interfaces are investigated using surface profiler or imaging equipments such as scanning tunneling microscopy (STM), atomic force microscopy (AFM), scanning electron microscopy (SEM) and TEM in order to quantify the

surface roughness. However, such analysis method as STM and AFM can characterize only the surface roughness of the nonporous materials or macroporous materials without tortuous, overlaid or deep pores. Recently, high resolution transmission electron microscopy (HRTEM) has been applied to evaluate the surface fractal dimensions $d_{surf}$ of the microporous carbon surfaces.[54,151-153] The most attractive point in this method is that the pores ranging in different sizes can be extracted from the TEM images which include contributions from many different pore sizes by the inverse fast Fourier transform (IFFT) operation by selecting the specific frequency range.

The surface fractal dimension $d_{surf}$ of the porous materials can be determined from the TEM image by using perimeter-area method[54,154-159]. If the scaling property of the porous materials is undoubtedly isotropic, the 3-D pore surface is simply related to the projection of the 3-D pore surface onto the 2-D surface. It is well known[154,155] that the area $A$ and the perimeter $P$ of the self-similar lakes are related to their self-similar fractal dimension $d_{F,ss}^{L}$ by

$$P = \beta_P d_{F,ss}^{L} A^{d_{F,ss}^{L}/2} \tag{26}$$

where $\beta_P$ is a proportionality constant. The surface fractal dimension of the original surface $d_{surf}$ is related to $d_{F,ss}^{L}$ by

$$d_{surf} = d_{F,ss}^{L} + 1 \tag{27}$$

In order to determine the value of $d_{surf}$, the original TEM image is digitized with the image scanner, and is then transformed to the binary images. For this, a low frequency cut off filter operation is performed along with fast Fourier transformation (FFT) to make the brightness uniform before the binary transformation, followed by the IFFT. The image is then transformed to its brightness on a scale from 0 to 255. Finally, any brightness larger than 128 is set at 255, and any brightness smaller than 127 is set at 0.

For instance, Figures 6a and 6b show the digitized TEM images of the mesoporous carbon specimen CAS30 prepared using silica imprinting method and the binary TEM images transformed from Figure 6a, respectively.[54] The TEM picture of the carbon specimen was digitized with the image scanner and then the data were transferred to $384 \times 384$ pixels. The digitized image size in

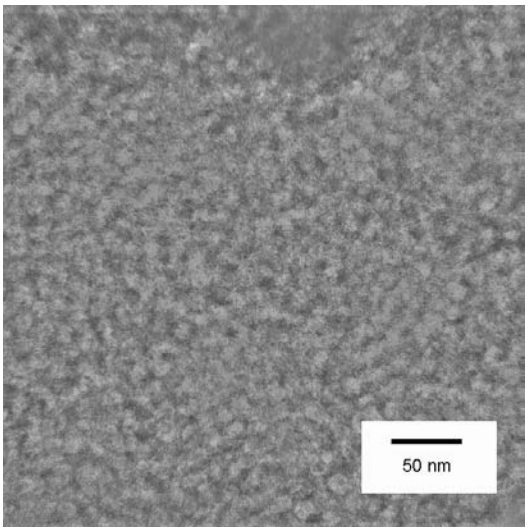



Figure 6. (a) The digitized TEM images of the mesoporous carbon specimen CAS30 prepared using silica imprinting method and (b) the binary TEM images transformed from (a). Reprinted with permission from S. -I. Pyun and C. -K. Rhee, *Electrochim. Acta*, **49** (2004) 4171. Copyright © 2004, With permission from Elsevier.

Figure 6a corresponds to an area of 400 × 400 $nm^2$, so that the image contains information about many pores.

Figure 7 demonstrates on a logarithmic scale the dependence of perimeter $P$ on area $A$ of the pores obtained from the binary TEM image of CAS30 in Figure 6b. The (log $P$ – log $A$) plots obtained from the carbon specimen displayed two straight lines with different slopes that can be divided into region I and II, indicating multifractal geometry of the carbon specimen. The individual surface fractal dimensions in regions I and II were determined from Eqs. (26) and (27) to be 2.08 $\pm$ 0.018 and 2.72 $\pm$ 0.046, respectively. The transition area $A_{tr}$ from region I to II were determined to be 108 $nm^2$, which corresponds to the pore diameter of 12 nm based upon spherical pore shape.

In Pyun and Rhee's work,[54] it should be emphasized that the pore diameter calculated from $A_{tr}$ is similar to the transition pore diameters between two groups of the carbonization-induced pores and the silica-imprinted pores in PSD. It is thus indicated that the

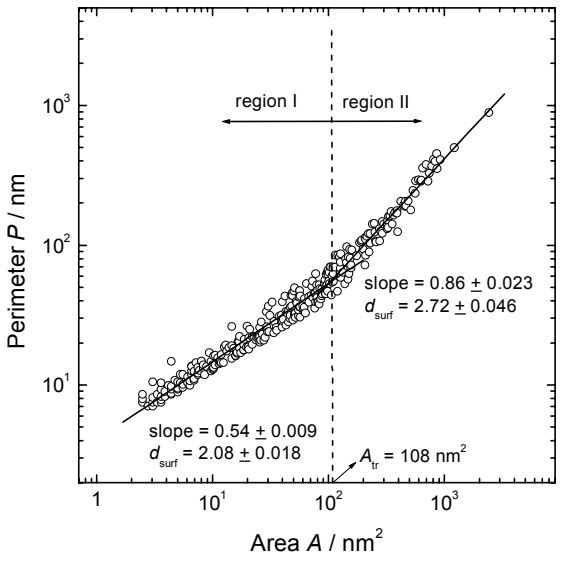



Figure 7. Dependence of perimeter $P$ on area $A$ of the lakes on a logarithmic scale obtained from the binary TEM images of CAS30 in Figure 6b. Reprinted with permission from Reprinted with permission from S. -I. Pyun and C. -K. Rhee, *Electrochim. Acta*, **49** (2004) 4171. Copyright © 2004, With permission from Elsevier.

values of $d_{surf}$ in regions I and II represent the individual surface fractal dimensions of the carbonization-induced pore surface and the silica-imprinted pore surface, respectively. From the comparison of the overall surface fractal dimension evaluated by the molecular probe method using gas adsorption with the individual fractal dimension, they concluded that the overall surface fractal dimension is crucially influenced by the individual dimension of the silica-imprinted pore surface.

As mentioned above, the advantage of the image analysis method is that the information of the pores in different size ranges can be extracted from the TEM images using IFFT operation by selecting the specific frequency range. By comparing the individual surface fractal dimension determined from the TEM images with the overall surface fractal dimension estimated by using other complementary methods, we can more specify the cutoff length scale of the surface fractality and examine the individual surface fractal dimension which dominantly influences the overall surface fractal dimension.

## V. ELECTROCHEMICAL CHARACTERISTICS OF CARBON-BASED POROUS ELECTRODES FOR SUPERCAPACITOR: THE USES OF AC-IMPEDANCE SPECTROSCOPY, CURRENT TRANSIENT AND CYCLIC VOLTAMMETRY

### 1. General Theory of Electrochemical Behavior of Porous Electrodes

The model to describe the electrochemical behavior of the porous electrode was first treated by De Levie.[160-162] He represented a pore surface by a transmission line as shown in Figure 8, and derived the following expression for the impedance of the pore, $Z_o$

$$Z_o = (1-j)\left(\frac{R'}{2\omega C'}\right)^{1/2} \coth\left[(1+j)\left(\frac{\omega R'C'}{2}\right)^{1/2} l_p\right] \tag{28}$$

with

$$R' = \frac{1}{k_e \pi r^2} \text{ and } C' = C_d 2\pi r \tag{29}$$

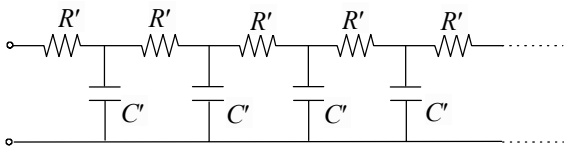



Figure 8. Equivalent circuit of a transmission line network representing the ion migration into the pores. $R'$ and $C'$ denote the resistance of the electrolyte inside a pore and the double-layer capacitance of the electrode/electrolyte interface, respectively, both of which are taken per unit length.

where $R'$ is the resistance of the electrolyte inside a pore per unit pore length; $C'$, the double-layer capacitance of the electrode/electrolyte interface per unit pore length; $\omega$, angular frequency; $l_p$, the pore length; $r$, the pore radius; $k_e$, the conductivity of the electrolyte, and $C_d$ represents the specific double-layer capacitance per unit area.

The assumptions of this model include the cylindrical pore shape, uniformly distributed $R'$ and $C'$, the lack of tortuosity of the pore, the lack of distributions of pore size and length, and no curvature of the equipotential surface in a pore. The resulting impedance spectra theoretically calculated based upon Eq. (28) is plotted in Figure 9. The straight inclined line at high frequencies is attributable to the semi-infinite ion migration through the pores. The capacitive line at low frequencies is due to the accumulation of ions at the bottom of the pores. At high frequencies, Eq. (28) reduces to

$$Z_o(\text{high freq.}) = (1-j)\left(\frac{R'}{2\omega C'}\right)^{1/2} \tag{30}$$

and the interfacial impedance has a phase angle of 45°, whereas at low frequencies Eq. (28) can be written as

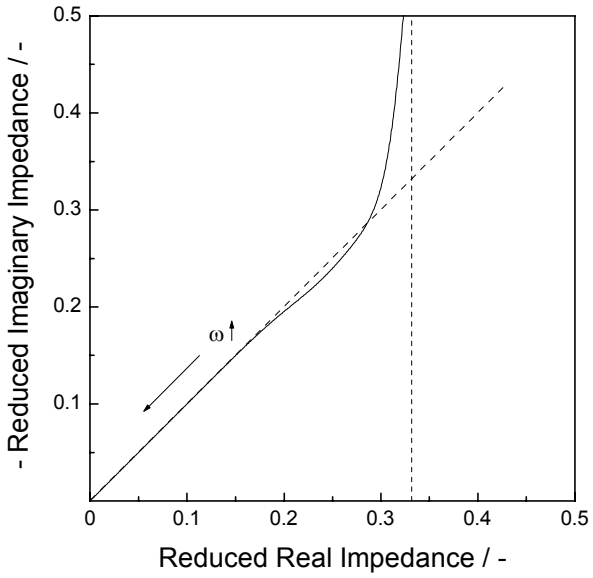



Figure 9. Nyquist plot of the impedance spectra of a cylindrical pore theoretically calculated with Eq. (28).

$$Z_o(\text{low freq.}) = \frac{1}{j\omega C' l_p} + \frac{R' l_p}{3} \tag{31}$$

and the phase angle tends towards 90°.

Although De Levie's work succeeds in explaining qualitatively the observed impedance behavior of the porous electrode, many assumptions and approximations limited the model's ability to represent accurately the measured impedance spectra. In particular, the impedance spectra experimentally measured on the porous carbon electrodes for EDLC do not show an ideal impedance behavior of a cylindrical pore. Over the years, such non-ideal impedance behavior of the porous electrode, i.e., frequency dispersion has been investigated by many researchers.[9,14-17,163-178] Generally, it has been suggested that the geometric heterogeneity such as pore shape and pore size/length distributions and surface inhomogeneity such as different crystallographic orientations and the SAFGs can cause time constant distributions, thus causing

frequency dispersion. The details are described in the following Sections V.2 and V.3.

## 2. Effect of Geometric Heterogeneity on Ion Penetration into the Pores during Double-Layer Charging/Discharging

The electrochemical impedance of a real electrode is frequently represented by an equivalent circuit containing constant phase element (CPE) showing power-law frequency dependence as follows

$$Z(\omega) = (1/C_{\mathrm{CPE}})(j\omega)^{-\alpha} \tag{32}$$

where $C_{\mathrm{CPE}}$ and $\alpha$ mean the CPE coefficient and the CPE exponent, respectively, and $\omega$ represents the angular frequency. Since the CPE or capacitance dispersion of the impedance spectra causes time constant distributions, and thus significantly influences the kinetics of double-layer charging/discharging of the porous electrode, it is necessary to understand the physical origins of the capacitance dispersion. It has been considered that one of the most possible causes of the CPE is known to be of geometric origin: An irregular and porous electrode geometry causes current density inhomogeneities and thus yields deviations from ideal capacitive behavior.

Keiser et al.[164] first showed that the more occluded the shape of the pore, the more distorted the impedance locus from the ideal capacitive behavior. However, the pore shapes in real system turn out to be much complicated and thus a straightforward analytical calculation is not usually possible of the overall impedance for those complicated pores. In connection with this problem, the fractal geometry has given a powerful tool for the analysis of the CPE behavior of the porous electrode. A number of theoretical papers[166,179-191] have devoted to investigate the relationship between the fractal geometry of the electrode and the CPE impedance on the basis of the electrolytic resistive distribution due to the surface irregularity.

Among various models proposed, a model of self-similar fractal electrode from Nyikos and Pajkossy[166] gives the following relation of the CPE exponent $\alpha$ to the self-similar fractal dimension $d_{\mathrm{F,ss}}$ as

$$\alpha = \frac{1}{d_{F,ss} - 1} \tag{33}$$

For a perfectly smooth surface with $d_{F,ss}$ = 2 at all scales, Eq. (33) predicts $\alpha$ = 1, i.e., purely capacitive behavior. In other limit as $d_{F,ss}$ = 3, $\alpha$ = 0.5 which is de Levie's well-known result for the electrode with cylindrical pore. Eq. (33) also implies that the surfaces with different morphologies but with same surface fractal dimension are equivalent as far as the impedance is concerned. The relationship between $d_{F,ss}$ and $\alpha$ is dependent upon the model used in the fractal characterization of the electrode.

However, Kerner and Pajkossy[167,171,176] have recently shown that for the electrode with microscopic roughness in aqueous electrolyte, the capacitance dispersion due to the surface irregularity should appear at such a high frequency range as kHz to GHz which is much higher than those frequencies at which the capacitance dispersion is usually experimentally observed. In their work, it was recognized that the capacitance dispersion is closely related to the surface inhomogeneity rather than surface irregularity. Pyun et al.[17,178] also suggested that the contribution of the surface inhomogeneity is much higher than the contribution of the surface irregularity to the capacitance dispersion on the porous carbon electrodes.

As a matter of fact, for porous carbon electrode it is still a troublesome issue to relate the determined surface fractal dimension $d_{F,ss}$ with the CPE exponent $\alpha$. The effect of the surface inhomogeneity on the ion penetration into the pores during double-layer charging/discharging will be discussed in detail in the following Section V.3.

In recent years it has been demonstrated by many researchers[16,172,173] that the frequency dispersion or capacitance dispersion is intimately related to PSD or pore length distribution (PLD). In this case, the frequency dispersion is not called 'CPE behavior' since the phase angle of the impedance spectra did not show a constant value over the whole frequency range. The phase angle of the impedance spectra measured on the porous electrode with broad PSD or PLD is larger than $45^o$ in value at high frequencies and smaller than $90^o$ in value at low frequencies.

Considering PSD or PLD, the total impedance of the pores, $Z_{tot}$ is given by

$$\frac{1}{Z_{\text{tot}}} = \int_{-\infty}^{\infty} \frac{1}{Z_{\text{o}}} f(x)dx \approx \sum_i \frac{1}{Z_{\text{o, i}}} f_i \Delta x_i \equiv \sum_i \frac{1}{Z_{\text{o, i}}} n_i \tag{34}$$

where $f(x)$ and $f(x)dx$ represent a distribution density function of PSD or PLD and the number of the pores between $x$ and $x + dx$, respectively.

Song et al.[172] theoretically calculated the impedance spectra based upon Eq. (34) with such distribution functions of PSD as normal, lognormal, Lorentzian, log Lorentzian distributions. They concluded that the impedance spectra simulated based upon the transmission line model (TLM) with different PSD functions share a common point that the wider PSD leads to the more frequency dispersion in the impedance spectra.

Recently, Lee et al.[16] investigated the effect of PLD on the kinetics of double-layer charging/discharging of the activated-carbon fiber cloth electrode (ACFCE). In order to disregard the effect of the pore shape on the electrochemical performance of the electrode, they used the ACFCE as an electrode material since the shape of the pores comprising the activated carbon fiber is cylindrical and homogeneous throughout the bulk of the fiber[152,192]. It is assumed that the pore length $l_{\text{p}}$ takes a lognormal distribution $f(x')$ as follows

$$f(x') = \frac{V_{\text{tot}}}{\pi r^2 l_{\text{p}}} \frac{1}{\sqrt{2\pi}\sigma} \exp\left[ -\frac{1}{2}\left( \frac{x'-\mu}{\sigma} \right)^2 \right] \tag{35}$$

with

$$x' = \ln(l_{\text{p}} / l_{\text{o}}) \tag{36}$$

where $x'$ denotes the natural logarithm of $l_{\text{p}}$ divided by an arbitrary unit pore length $l_{\text{o}}$ to obtain a dimensionless quantity; $V_{\text{tot}}$, the total pore volume; $\mu$ and $\sigma$ are the mean value and the standard deviation of the distribution variable $x'$, respectively.

Substituting $y = \dfrac{x'-\mu}{\sigma}$ into Eq. (35), we get

$$f(y) = \frac{V_{\text{tot}}}{\pi r^2 l_{\text{p}}} \frac{1}{\sqrt{2\pi}} \exp\left( -\frac{1}{2} y^2 \right) \tag{37}$$

Hence, the $Z_{tot}$ leads to

$$\frac{1}{Z_{tot}} = \int_{-\infty}^{\infty} \frac{1}{Z_o} f(y)dy = \int_{-\infty}^{\infty} \frac{1}{Z_o} \frac{V_{tot}}{\pi r^2 l_p} \frac{1}{\sqrt{2\pi}} \exp\left(-\frac{1}{2}y^2\right)dy \quad (38)$$

with

$$\int_{-\infty}^{\infty} \frac{1}{\sqrt{2\pi}} \exp\left(-\frac{1}{2}y^2\right)dy = 1 \quad (39)$$

From the quantitative coincidence of the impedance spectrum experimentally measured with that theoretically calculated with Eq. (38) as depicted in Figure 10, they suggested that such non-ideal

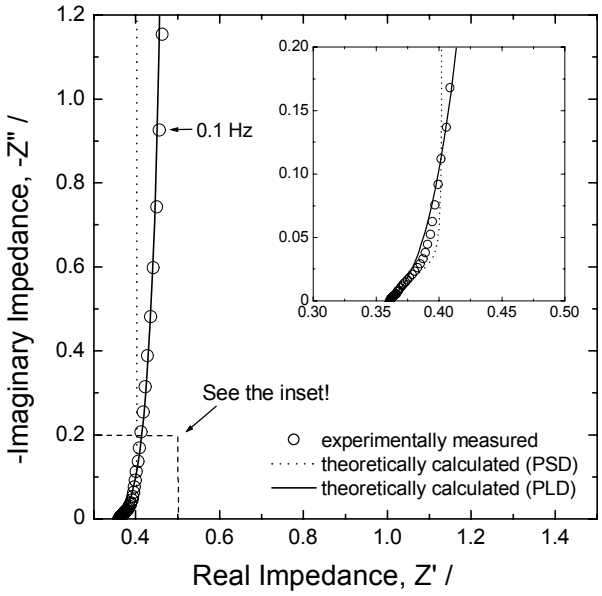



Figure 10. Nyquist plot of the impedance spectrum experimentally measured on the ACFCE at an applied potential of 0.1 V (*vs.* SCE) in a 30 wt % $H_2SO_4$ solution. Dotted and solid lines represent the impedance spectra theoretically calculated based upon the transmission line model (TLM) in consideration of pore size distribution (PSD) and pore length distribution (PLD), respectively. Reprinted with permission from G. -J. Lee, S. -I. Pyun, and C. -H. Kim, *J. Solid State Electrochem.*, **8** (2004) 110. Copyright © 2003, with kind permission of Springer Science and Business Media.

impedance behavior of the ACFCE is mainly due to PLD, rather than due to PSD.

When PLD is considered together with the solution resistance $R_{sol}$, between reference electrode (R.E.) and working electrode (W.E.), the total current $I_{tot}(t)$ is written as

$$I_{tot}(t) = \int I(t) f(y) dy \tag{40}$$

$$= \int \frac{2\Delta E}{R_{sol}} \sum_{n=1}^{\infty} \frac{\Lambda}{\Lambda^2 + \Lambda + m_n^2} \times \exp\left( - m_n^2 k_e r t \Big/ 2 C_d {l_p}^2 \right) \frac{V_{tot}}{\pi r^2 l_p} \frac{1}{\sqrt{2\pi}} \exp(-\frac{1}{2} y^2) dy$$

with

$$\Lambda = \frac{R_p}{R_{sol}} \text{ and } R_{sol} = \frac{l_s}{k_e \pi r^2} \tag{41}$$

where $\Delta E$ is the potential step; $R_p$, the resistance of the electrolyte inside a pore; $l_s$, the distance between R.E. and W.E.; $m_n$, the $n$th positive root of ($m$ tan $m - \Lambda = 0$); $f(y)$ and $f(y)dy$ represent a distribution density distribution of the pore length and the number of the pores between $y$ and $y + dy$, respectively.

Lee et al.[16] theoretically calculated the cathodic current transients based upon the TLM as a function of σ of PLD. Figures 11a and 11b illustrate the logarithmic cathodic current transients and the derivatives of the logarithmic cathodic current transients calculated from Eq. (40) with the change of σ of PLD, respectively. It is noted that as σ increases, the current decays more rapidly with time due to the dominant contribution of the pores with smaller length in the region I, whereas the current decays more slowly with time due to the dominant contribution of the pores with larger length in the region II.

In the case of potential scanning with a scan rate ν, in consideration of PLD, the total current $I_{tot}(t)$ is given by

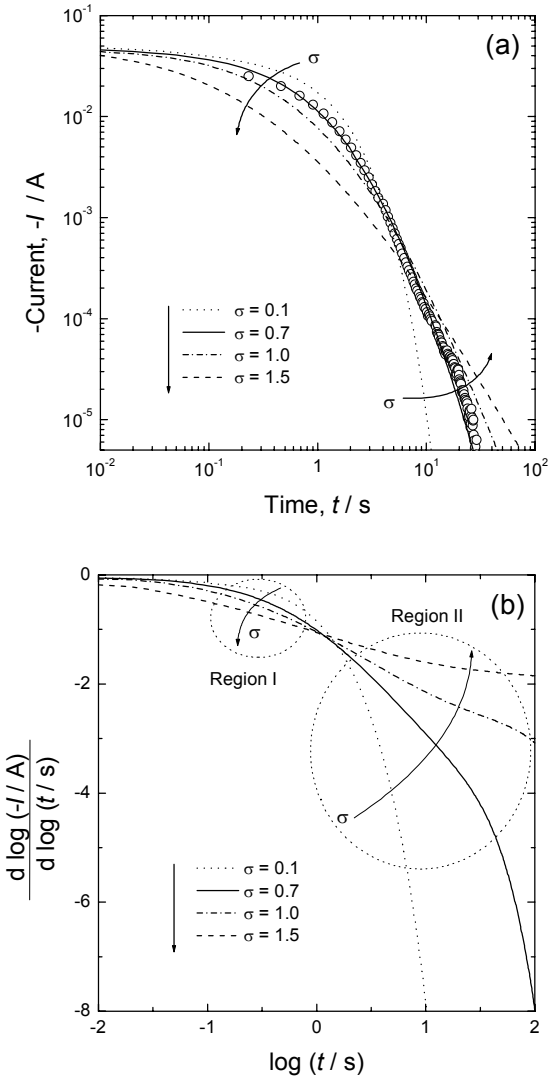



Figure 11. (a) The cathodic current transients on a logarithmic scale and (b) the derivatives of the logarithmic cathodic current transients theoretically calculated from Eq. (40) based upon the TLM as a function of standard deviation σ of PLD. Open circles in Figure 11 represent the cathodic current transient experimentally measured on the ACFCE. Reprinted with permission from G. -J. Lee, S. -I. Pyun, and C. -H. Kim, *J. Solid State Electrochem.*, **8** (2004) 110. Copyright © 2003, with kind permission of Springer Science and Business Media.

$$I_{\text{tot}}(t) = \int I(t) f(y) dy \tag{42}$$

$$= \int (\beta_1 - \beta_2) \nu C_{\text{d}} 2\pi r l_{\text{p}} \frac{V_{\text{tot}}}{\pi r^2 l_{\text{p}}} \frac{1}{\sqrt{2\pi}} \exp\left(-\frac{1}{2} y^2\right) dy$$

with

$$\beta_1 = 1 - \sum_{n=1}^{\infty} \frac{2\Lambda^2}{m_n^2[\Lambda^2 + \Lambda + m_n^2]} \exp\left(-m_n^2 k_{\text{e}} rt \Big/ 2C_{\text{d}} l_{\text{p}}^2\right) \tag{43}$$

$$\beta_2 = \sum_{n=1}^{\infty} \left(\frac{\Lambda^2 + m_n^2}{\Lambda^2 + \Lambda + m_n^2}\right) \exp\left(-m_n^2 k_{\text{e}} rt \Big/ 2C_{\text{d}} l_{\text{p}}^2\right) \left(\frac{2}{m_n^2}\right) \sin^2 m_n \tag{44}$$

The rate capability $\gamma_{\text{cap}}$ defined as the quotient of the reduced charge for the ACFCE divided by the reduced charge for the ideal double layer capacitor increased with increasing $\sigma$ of PLD, as shown in Figure 12. Consequently, from the above theoretical and experimental results, it is concluded that the ion penetration into the pores during double-layer charging/discharging is more impeded as $\sigma$ of PLD increases.

## 3. Effect of Surface Inhomogeneity on Ion Penetration into the Pores during Double-Layer Charging/Discharging

It has been reportedly known[17,178,193-198] that for the carbon electrodes the basal and edge planes are randomly distributed on the electrode surface and the values of the specific double-layer capacitance per unit area $C_{\text{d}}$ range from about 1 μF cm$^{-2}$ for the basal planes to about 70 μF cm$^{-2}$ for the edge planes. The conductive and capacitive properties of the basal and edge planes are different from each other. Along the direction of the edge planes, the carbon specimen can be treated as a conductor, while it shows the properties of semiconductor along the direction of the basal planes. These randomly distributed capacitive elements give rise to the distribution in the current density along the electrode surface.

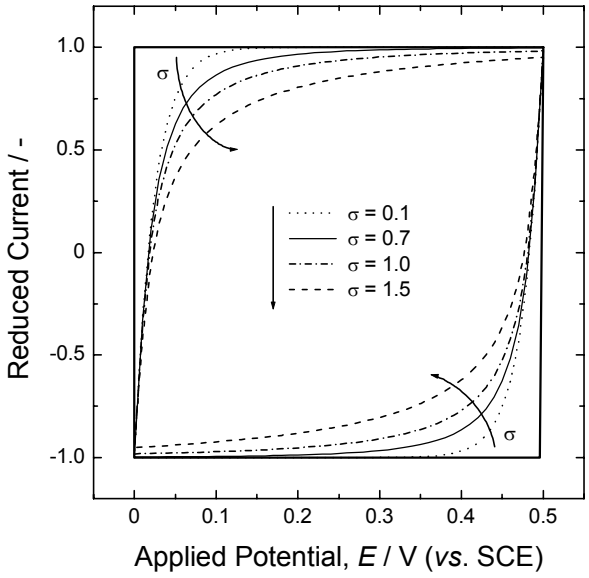



Figure 12. Plots of the reduced current against the applied potential theoretically calculated based upon the TLM as functions of σ of PLD at a scan rate of 20 mV $s^{-1}$. Solid bold line denotes the ideal double-layer capacitor where the time constant is zero. Reprinted with permission from G. -J. Lee, S. -I. Pyun, and C. -H. Kim, *J. Solid State Electrochem.*, **8** (2004) 110. Copyright © 2003, with kind permission of Springer Science and Business Media.

Furthermore, the basal plane is flat on the atomic scale and can be considered as a nearly perfect single crystal since there are no unsaturated chemical bonds, free electrons and/or SAFGs. On the other hand, the edge planes are associated with unpaired electrons or have residual valencies which are very active. Therefore, various defects or SAFGs are bound to the edge planes, causing more increase in the surface inhomogeneity. The surface inhomogeneities resulting from these crystallographic orientations can cause time constant distributions, and hence they may influence the capacitance dispersion.

Recently, Lee and Pyun[17] have intensively investigated the effect of microcrystallite structures on electrochemical characteristics of the mesoporous carbon electrodes for EDLC. They effectively controlled the microcrystallite sizes of the carbon specimens in *a*- and *c*-axis direction, i.e., $L_a$ (parallel to the basal

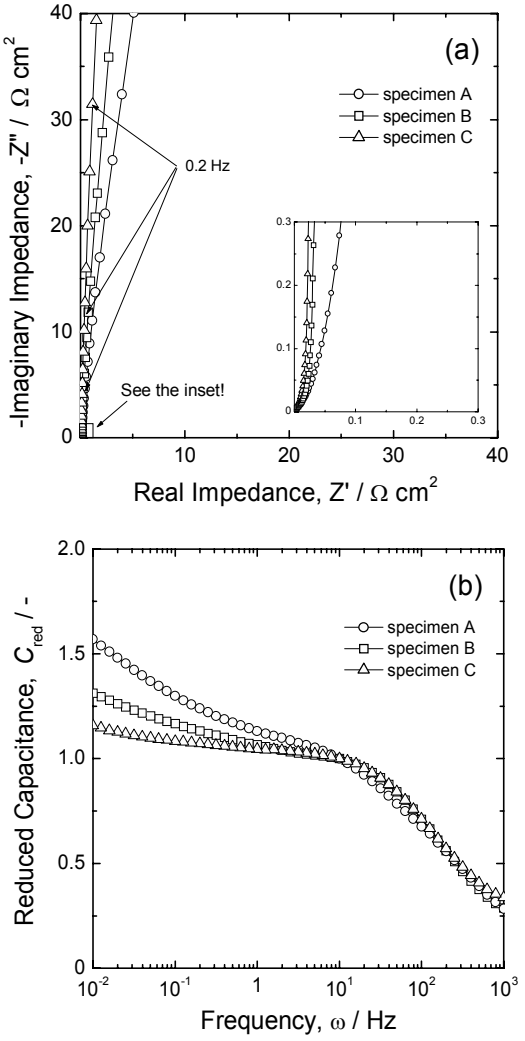



Figure 13. (a) Nyquist plots of the impedance spectra and (b) plots of reduced capacitance $C_{red}$ *vs*. frequency $\omega$ experimentally measured on carbon specimens A (-○-), B (-□-), and C (-Δ-) at an applied potential of 0.2 V (vs. SCE) in a 30 wt.% $H_2SO_4$ solution. Here, the solution resistance was subtracted from the measured impedance spectra. The reduced capacitance in (b) was determined from the normalization of the capacitance with respect to the value of the capacitance calculated from the impedance spectra at 10 Hz. Reprinted from Ref. [17], Copyright (2006), with permission from Elsevier.

planes) and $L_c$ (parallel to the edge planes) by using different carbonaceous precursors with various heat-treatment temperatures.

The impedance spectra measured on three kinds of carbon specimens exhibited the CPE behavior in low frequencies (Figure 13a), and the frequency dispersion of the impedance spectra at low frequencies increased in the order of specimens C, B, and A (Figure 13b). The CPE exponent $\alpha$ decreased with increasing $L_c/L_a$, i.e., with increasing surface inhomogeneity as listed in Table 2. From their work, it is strongly indicated that the value of $\alpha$ is closely related to the amounts of the edge planes, that is, the frequency dispersion of capacitance increases with increasing surface inhomogeneity due to the wider time constant distribution. Furthermore, it is also found from Table 2 that the value of $C_d$ calculated at the lowest frequency, i.e., $10^{-2}$ Hz in the impedance spectra increased with increase in $L_c/L_a$, which is due to the higher value of $C_d$ for the edge planes than that for the basal planes.

For the time domain responses of the CPE, the current density difference ($\Delta i$)/scan rate ($\nu$) relation is expressed by the following power-law during the potential scanning[199]

$$\Delta i \propto \nu^{\alpha} \tag{45}$$

where $\Delta i$ represents the difference in current density between anodic and cathodic peak currents of the CVs.

Figure 14 gives on a logarithmic scale the variations of $\Delta i$ of the CVs experimentally measured on the carbon electrodes as a function of the scan rate $\nu$.[17] For specimens A, B, and C, $\Delta i$ of the CVs were linearly proportional to the scan rate $\nu$ to the power of 0.894, 0.916, and 0.942, respectively, which are slightly smaller than those values of $\alpha$ determined from the impedance spectra. From the qualitative coincidence between the values of $\alpha$ determined from the impedance spectra and the CVs, it is suggested that the distributive characteristics of the capacitance in the frequency domain greatly influence the capacitance dispersion in the time domain which is related to the kinetics of double-layer charging/discharging.

Figure 15 presents the plots of the rate capability $\gamma_{cap}$ against the scan rate $\nu$ calculated from the CVs experimentally measured on carbon specimens A, B, and C.[17] The higher the value of $L_c/L_a$ was, the lower exhibited the rate capability $\gamma_{cap}$, regardless of the scan rate $\nu$. Besides, as $L_c/L_a$ increased, the rate capability $\gamma_{cap}$

**Table 2.**
**The Mass of the Electrode *m*, the BET Surface Area $A_{BET}$, the Total Pore Volume $V_{tot}$, the Average Pore Diameter $D_{ave}$, the Size of the Microcrystallite $L_a$ (Parallel to the Basal Plane), $L_c$ (Parallel to the Edge Plane), the Ratio of $L_c/L_a$, the CPE Exponent α and the Specific Double-Layer Capacitance $C_d$ for Carbon Specimens A, B and C. Reprinted from Ref. [17], Copyright (2006), with permission from Elsevier.**

| Specimen | Mass of the electrode, *m* (mg) | BET surface area, $A_{BET}$ ( $m^2 g^{-1}$) | Total pore volume, $V_{tot}$ ($cm^3 g^{-1}$) | Average pore diameter, $D_{ave}$ (nm) | $L_a$ (nm) | $L_c$ (nm) | $L_c/L_a$ /- | CPE exponent α /- | Specific double-layer capacitance, $C_d$ ( $F m^{-2}$) |
|---|---|---|---|---|---|---|---|---|---|
| A | 1.33 | 750 | 1.80 | 12.4 | 1.6 | 1.3 | 0.81 | 0.919 | 0.20 |
| B | 2.53 | 394 | 1.39 | 12.0 | 1.9 | 1.2 | 0.63 | 0.945 | 0.11 |
| C | 2.10 | 477 | 1.46 | 11.2 | 3.9 | 2.0 | 0.51 | 0.964 | 0.04 |

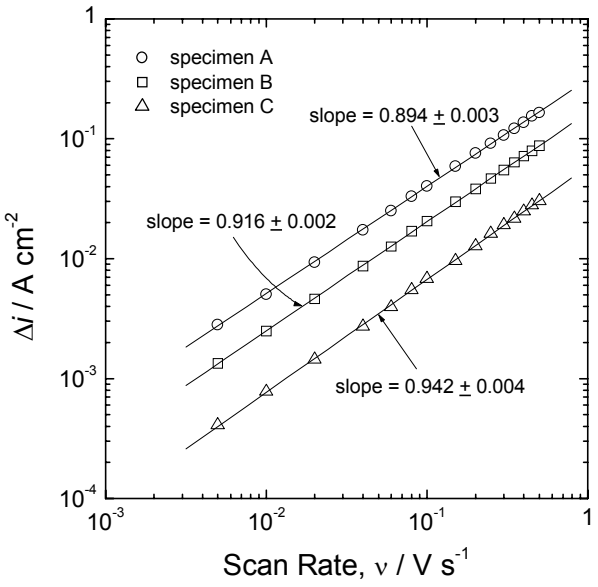



Figure 14. Dependence of the current density difference $\Delta i$ between anodic and cathodic peak currents of the cyclic voltammograms (CVs) on the scan rate ν for carbon specimens A (○), B (□), and C (Δ). Reprinted from Ref. [17], © (2006), with permission from Elsevier.

decayed more rapidly with the scan rate ν. From the above results, it is concluded that the ion penetration into the pores is more impeded with increasing surface inhomogeneity, which is attributable to both the higher value and wider distribution of the time constant.

It has been generally reported[14,196,200-203] that the chemical heterogeneities (SAFGs) significantly influence the electrochemical performance of the porous carbon electrodes. The SAFGs are mostly bound to lateral planes (edges of the aromatic sheet) of the carbon electrode, because these sites are associated with unpaired electrons or have residual valencies which are very reactive. The SAFGs contribute to the increase in the total capacitance of EDLC,[203] and the electrolyte wettability can be improved by increasing amounts of the oxygen content associated with hydrophilic surface groups.[204] However, the presence of the SAFG

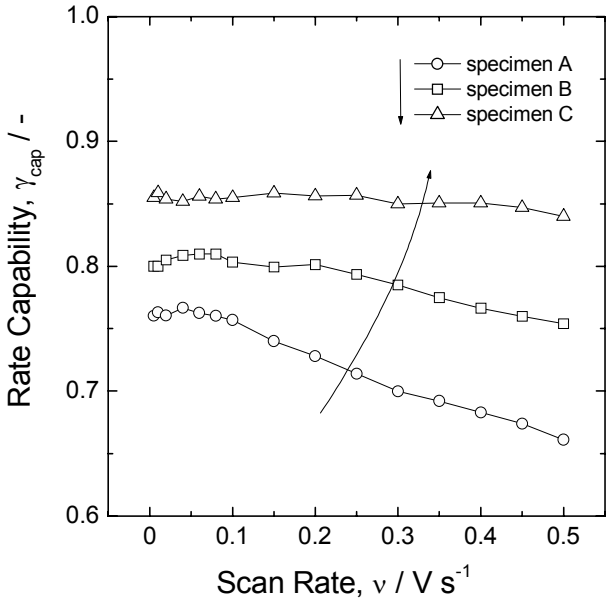



Figure 15. Plots of the rate capability $\gamma_{cap}$ against the scan rate $\nu$ calculated from the CVs experimentally measured on carbon specimens A (○), B (□), and C (Δ). Reprinted from Ref. [17], Copyright (2006), with permission from Elsevier.

on the carbon surface is not always beneficial since they serve to increase the leakage current.[205]

The SAFGs formed on the carbon electrode are the intermediate product of such gaseous oxides as CO and $CO_2$ appearing as final carbon oxidation products. The concentration of the SAFG increases with an increase in the oxidation temperature and reaches a maximum at 400 $^{o}$C to 500 $^{o}$C. At higher temperatures, the SAFG is thermally unstable and hence decomposes to CO and $CO_2$ gases.[196,197] The SAFGs can be also formed on the carbon electrode by electrochemical activation. Sullivan et al.[202] electrochemically activated the glassy carbon electrodes at 1.85 to 2.05 V (*vs*. SCE) and then reduced at –0.2 to –0.4 V (vs. SCE) in sulfuric acid solution. During repetitive activation/reduction processes, the large amounts of the SAFGs were formed on the glassy carbon electrodes and those SAFGs

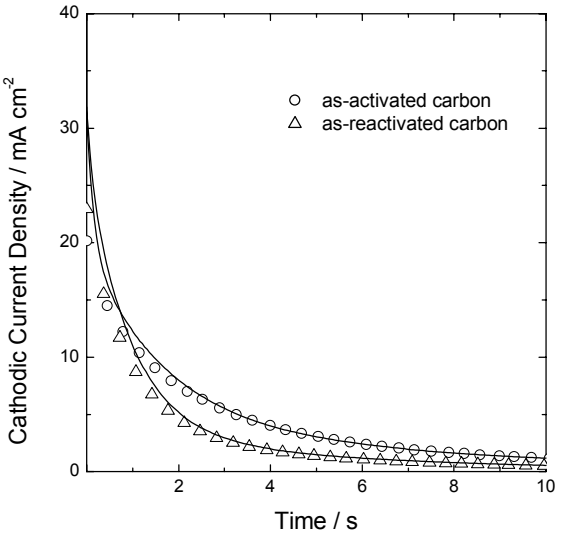



Figure 16. The cathodic current transients experimentally obtained from the as-activated carbon (○) and as-reactivated carbon (Δ) electrode specimens in a 30 wt.% $H_2SO_4$ solution by dropping the applied potential from 0.1 to 0.08 V (*vs*. SCE). Solid lines represent the simulated cathodic current transients. Reprinted with permission from C.-H. Kim, S.-I. Pyun, and H.-C. Shin, *J. Electrochem. Soc.* **149** (2002) A93. Copyright © 2001, with permission from The Electrochemical Society.

significantly affected the impedance spectra and the CVs in shape and value, depending upon the potential. It has been reported[200-202] that the double-layer capacitance which is related to the state of protonation of the SAFGs is strongly dependent upon the potential and exhibits the maximum value in potential ranges between 0.3 and 0.5 V (*vs*. SCE).

Kim et al.[14] have attempted to investigate the role of the SAFG in the kinetics of double-layer charging/discharging of activated carbon powder electrode specimens. In order to leave the effect of PSD out of consideration, they prepared two kinds of as-activated and as-reactivated carbon powder specimens, which are characterized by almost the same PSD, but by different concentration of the oxygen functional groups. The concentration of the oxygen functional groups of the as-activated carbon powder

specimen was measured to be 1.35 mmol $g^{-1}$ which is much higher in value than that of the as-reactivated carbon powder specimen (0.34 mmol $g^{-1}$).

The cathodic current transients (designated as open symbols) experimentally determined from the as-activated and as-reactivated carbon electrode specimens are given in Figure 16, together with those simulated (designated as solid lines). The simulation was performed from the circuit analysis using the SPICE based upon the six-RC-element ladder network at a potential step by taking the values of circuit elements obtained from the complex nonlinear least-squares (CNLS) fitting method of experimental impedance spectra. For the as-activated carbon electrode specimen, the current density decayed more slowly with time than that for the as-reactivated carbon electrode specimen due to higher time constant for the former carbon electrode specimen than that for the latter carbon electrode specimen.

In Figure 17, the rate capability $\gamma_{cap}$ was determined to be 0.60 for the as-activated carbon electrode specimen. This value is lower than that for the as-reactivated carbon electrode specimen 0.76. From these results, it is confirmed that the SAFG reduces the ion penetration depth, and hence impedes the ion penetration into the pores during double layer charging of the carbon electrodes.

## VI. CONCLUDING REMARK

The present article first provided the brief overview of the synthetic methods of the porous carbons. In order to prepare the microporous carbons with high surface area, the physical/chemical activation methods have been widely used for a long time.[18-35] Recently, the meso/macroporous carbons with various pore structures are prepared by templating methods by using various templates and changing sol-gel reaction conditions, e.g., pH, amount of template, and gelation temperature.[17,36-55]

Subsequently, the characterization of the pore structures of the porous materials using gas adsorption method was discussed in detail. The types and characteristics of the adsorption isotherms and the hysteresis loops were introduced. In addition, the BET (Braunauer, Emmett, and Teller) theory[92] for the determination of the surface area and various theoretical models for characterization of the pore structures according to the pore size range were summarized based upon the adsorption theory.

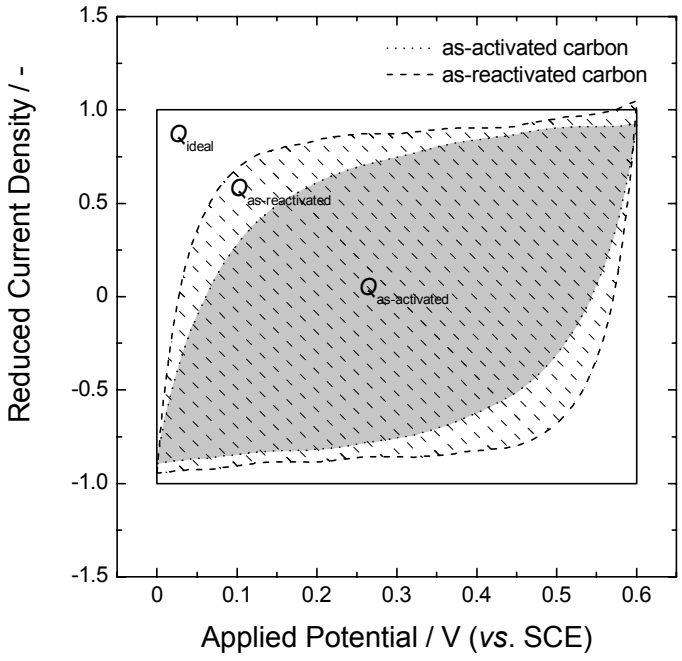



Figure 17. Plots of the reduced current density against the applied potential obtained from the as-activated carbon (dotted line) and as-reactivated carbon (dashed line) electrode specimens. Solid line represents the ideal double layer capacitor where the time constant is zero. Reprinted from C.-H. Kim, S.-I. Pyun, and H.-C. Shin, *J. Electrochem. Soc.* **149** (2002) A93. Copyright © 2001, with permission from The Electrochemical Society.

And then, the molecular probe method and the image analysis method for quantitative characterization of pore surface irregularity and size distribution irregularity were discussed based upon the fractal theory. The surface fractal dimensions[56,58,65] which characterize the pore surface irregularity were successfully determined by the multiprobe (MP) method[56,117,120-133] that uses several kinds of multiprobe molecules with different molecular sizes and the single-probe (SP) method[56,58,60,137,138] based upon the modified FHH (Frenkel,[139] Halsey,[140] and Hill[141]) theory describing multilayer gas adsorption.

On the other hand, for the microporous carbons with pore size distribution (PSD) with pore fractality, the pore fractal dimensions[56,59,62] which represent the size distribution irregularity can be theoretically calculated by non-linear fitting of experimental adsorption isotherm with Dubinin-Astakhov (D-A) equation in consideration of PSD with pore fractality.[143-149] The image analysis method[54,151-153] has proven to be also effective for the estimation of the surface fractal dimension of the porous materials using perimeter-area method.[154-159]

Finally, as electrochemical applications of the porous carbons to electrode materials for supercapacitor, this review covered the effects of geometric heterogeneity and surface inhomogeneity on ion penetration into the pores during double-layer charging/ discharging. It is noted that for the reliable fractal characterization of the pore surfaces in terms of the constant phase element (CPE) exponent $\alpha$, it must be rigorously checked whether the surface state of the electrode is homogeneous or not and whether the effect of the surface roughness on the CPE is more dominant rather than that of the surface inhomogeneity or not.

From the theoretical and experimental findings, it is obvious that the wider PSD or pore length distribution (PLD) leads to the more time constant distribution, thus causing higher retardation of ion penetration into the pores during double-layer charging/ discharging. Furthermore, it is recognized that the surface inhomogeneities such as microcrystallite sizes and the surface acidic functional groups (SAFGs) impede the ion penetration into the pores during double-layer charging/discharging of the carbon electrodes, and hence decrease the rate capability $\gamma_{cap}$.

## ACKNOWLEDGEMENTS

This work was supported by a grant from the Center for Advanced Materials Processing (CAMP) of the 21st Century Frontier R&D Program funded by the Ministry of Commerce, Industry and Energy (MOCIE), Republic of Korea. Furthermore, this work was partly supported by the Brain Korea 21 project.

## NOTATION

| | |
|---|---|
| $a_o$ | Diameter of adsorbed molecule |
| $A$ | Area |
| $A_{ad}$ | Adsorption potential |
| $A_{BET}$ | Total Braunauer, Emmett, and Teller (BET) surface area |
| $A_c$ | Molecular cross-sectional area |
| $A_{tr}$ | Transition area at which the linear relationship between the logarithm of perimeter and the logarithm of area changes |
| $\alpha$ | Constant phase element (CPE) exponent |
| ACFCE | Activated carbon fiber cloth electrode |
| AFM | Atomic force microscopy |
| $\beta$ | Affinity coefficient |
| $\beta_P$ | Proportionality constant in the relationship between the area and the perimeter |
| BDDT | Braunauer, Deming, Deming, and Teller |
| BET | Braunauer, Emmett, and Teller |
| BJH | Barrett, Joyner, and Halenda |
| $C$ | Constant in BET equation |
| $C'$ | Double-layer capacitance of the electrode/electrolyte interface per unit pore length |
| $C_{CPE}$ | CPE coefficient |
| $C_d$ | Specific double-layer capacitance per unit area |
| $C_{red}$ | Reduced double-layer capacitance |
| $C_{SP}$ | Power-law exponent which is dependent upon the surface fractal dimension determined by using the single-probe method using gas adsorption |
| CNLS | Complex nonlinear least-squares |
| CPE | Constant phase element |
| CV | Cyclic voltammogram |
| $D_{F.ss}$ | Self-similar fractal dimension |
| $d_{F,SS}^{L}$ | Self-similar fractal dimension of the two-dimensional self-similar lakes |
| $d_{pore,SP}$ | Pore fractal dimension determined by using the single-probe method using gas adsorption |
| $d_{surf}$ | Surface fractal dimension |
| $d_{surf,MP}$ | Surface fractal dimension determined by using the multiprobe method using gas adsorption |
| $d_{surf,SP}$ | Surface fractal dimension determined by using the single-probe method using gas adsorption |

| | |
|---|---|
| $D$ | Pore diameter |
| $D_{ave}$ | Average pore diameter |
| D-A | Dubinin-Astakhov |
| D-R | Dubinin- Radushkevich |
| $E$ | Potential |
| $E_o$ | Characteristic adsorption potential for the reference vapor, benzene |
| $\Delta E$ | Potential step |
| $\varepsilon$ | Threshold for the dominant forces between van der Waals forces and the liquid/gas surface tension forces in the multilayer gas adsorption |
| EDLC | Electric double-layer capacitor |
| $f(x)$ | Distribution density function of pore size distribution or pore length distribution |
| $f(x)dx$ | Number of the pores between $x$ and $x + dx$ |
| $f_P(x)$ | Fractal pore size distribution |
| FFT | Fast Fourier transform |
| FHH | Frenkel, Halsey, and Hill |
| $\Delta G$ | Gibbs' free energy |
| $\gamma$ | Incomplete gamma function |
| $\gamma_{cap}$ | Rate capability |
| $\gamma_L$ | Liquid surface tension |
| HRTEM | High resolution transmission electron microscopy |
| H-K | Horvath-Kawazoe |
| $I$ | Current |
| $I_{tot}$ | Total current |
| $\Delta i$ | Current density difference between anodic and cathodic peak currents of the cyclic voltammogram |
| IFFT | Inverse fast Fourier transform |
| IUPAC | International Union of Pure and Applied Chemistry |
| $j$ | $\sqrt{-1}$ |
| $k$ | Empirical constant |
| $k_e$ | Conductivity of the electrolyte |
| $l_o$ | Arbitrary unit pore length |
| $l_p$ | Pore length |
| $l_s$ | Distance between reference electrode and working electrode |
| $L_a$ | Microcrystallite sizes in $a$- axis direction (parallel to the basal planes) |
| $L_c$ | Microcrystallite sizes in $c$- axis direction (parallel to the edge planes |
| $m$ | Mass |

| | |
|---|---|
| $m_n$ | $n$th positive root of $(m \tan m - \Lambda) = 0$ |
| $\mu$ | Mean value of the distribution variables |
| MP | Multiprobe |
| $n$ | Equation parameter in Dubinin-Astakhov equation |
| $n_{ad}$ | Number of adsorbed molecule layers |
| $N_A$ | Avogadro constant |
| $N_{mono}$ | Number of adsorbed molecules to form a monolayer |
| $\nu$ | Potential scan rate |
| $p$ | Adsorption equilibrium pressure of the gas |
| $p^o$ | Saturation pressure of the gas |
| $p^*$ | Critical condensation pressure of the gas |
| $P$ | Perimeter |
| pH | Potential of hydrogen |
| PLD | Pore length distribution |
| PSD | Pore size distribution |
| $Q$ | Reduced charge |
| $Q_1$ | Enthalpy (heat) of adsorption in the first adsorbed layer |
| $Q_L$ | Enthalpy (heat) of liquefaction of adsorbate |
| $r$ | Pore radius |
| $r_1$ | First radius of curvature of the liquid meniscus in the pores |
| $r_2$ | Second radius of curvature of the liquid meniscus in the pores |
| $r_{ave}$ | Average pore radius |
| $r_{L,m}$ | Mean radius of curvature of the liquid meniscus |
| $r_m$ | Radius of the sphere probe molecule |
| $r_{max}$ | Pore radius of the maximum differential pore volume |
| $r_p$ | Radius of a cylindrical pore |
| $R$ | Gas constant |
| $R'$ | Resistance of the electrolyte inside a pore per unit pore length |
| $R_p$ | Resistance of the electrolyte inside a pore |
| $R_{sol}$ | Solution resistance between reference electrode and working electrode |
| R.E. | Reference electrode |
| $\sigma$ | Standard deviation of the distribution variables |
| SAFG | Surface acidic functional group |
| SCE | Saturated calomel electrode |
| SEM | Scanning electron microscopy |
| SP | Single-probe |
| SPICE | Simulation program with integrated circuit emphasis |

| | |
|---|---|
| STM | Scanning tunneling microscopy |
| $t$ | Time |
| $t_{ad}$ | Actual thickness of adsorbed molecule layers |
| $t_{ad,max}$ | High-end thickness of the fractal regime |
| $t_{ad,min}$ | Low-end thickness of the fractal regime |
| $T$ | Absolute temperature |
| $\theta$ | Contact angle between the solid and condensed phase |
| $\theta_L$ | Local adsorption isotherm |
| $\Theta$ | Overall adsorption isotherm |
| TEM | Transmission electron microscope |
| TEOS | Tetraethoxy silane |
| TLM | Transmission line model |
| TMOS | Tetramethoxy silane |
| $V$ | Volume of adsorbed gas molecule |
| $V_{cond}$ | Molar volume of the condensed adsorbate |
| $V_m$ | Molar volume of the gas |
| $V_{max}$ | Upper limits of the power-law regimes in the plot of ln $V$ against ln ln($p^o/p$) |
| $V_{min}$ | Lower limits of the power-law regimes in the plot of ln $V$ against ln ln($p^o/p$) |
| $V_{mono}$ | Volume of monolayer coverage |
| $V_o$ | Total micropore volume |
| $V_{tot}$ | Total pore volume |
| $w_p$ | Width of a parallel-sided slit |
| $\omega$ | Angular frequency |
| W.E. | Working electrode |
| $x$ | Average half-width of the slit-shaped pores |
| $x'$ | Natural logarithm of pore length $l_p$ divided by an arbitrary unit pore length $l_o$ to obtain a dimensionless quantity |
| $x_{max}$ | Upper limits of the pore fractality |
| $x_{min}$ | Lower limits of the pore fractality |
| $Z$ | Electrochemical impedance |
| $Z'$ | Real impedance |
| $Z''$ | Imaginary impedance |
| $Z_o$ | Impedance of the pore |
| $Z_{tot}$ | Total impedance of the pores |

## REFERENCES

[1]A. Adachi and T. Kobayashi, *Bull. Environ. Contam. Toxicol*. **54** (1995) 440.
[2]K. Kaneko, *Stud. Surf. Sci. Catal*. **120** (1998) 635.
[3]J. Sun, M. J. Rood, and A.A. Lizzio, *Gas Sep. Purif*. **10** (1996) 91.
[4]S. Sircar, T. C. Golden, and M. B. Rao, *Carbon* **34** (1996) 1.
[5]J.M. Martín-Martínez, L. Singoredjo, M. Mittelmeijer-Hazeleger, F. Kapteijn, and J. A. Moulijn, *Carbon* **32** (1994) 897.
[6]D. Mehandjiev, E. Bekyarova, and M. Khristova, *J. Colloid Interface Sci.* **192** (1997) 440.
[7]S. V. Mikhalovsky and Yu. P. Zaitsev, *Carbon* **35** (1997) 1367.
[8]M. Nakamura, M. Nakanishi, and K. Yamamoto, *J. Power Sources* **60** (1996) 225.
[9]D. Qu and H. Shi, *J. Power Sources* **74** (1998) 99.
[10]B.E. Conway, *Electrochemical Supercapacitors: Scientific Fundamentals and Technological Applications*, Kluwer Academic/Plenum Publishers, New York, 1999.
[11]G. Salitra, A. Soffer, L. Eliad, Y. Cohen, and D. Aurbach, *J. Electrochem. Soc.* **147** (2000) 2486.
[12]K. Honda, T. N. Rao, D. A. Tryk, A. Fujishima, M. Watanabe, K. Yasui, and H. Masuda, *J. Electrochem. Soc.* **148** (2001) A668.
[13]M. Endo, T. Maeda, T. Takeda, Y. J. Kim, K. Koshiba, H. Hara, and M. S. Dresselhaus, *J. Electrochem. Soc.* **148** (2001) A910.
[14]C. -H. Kim, S. -I. Pyun, and H. -C. Shin, *J. Electrochem. Soc.* **149** (2002) A93.
[15]S. -I. Pyun, C. -H. Kim, S. -W. Kim, and J. -H. Kim, *J. New Mat. Electrochem. Systems* **5** (2002) 289.
[16]G. -J. Lee, S. -I. Pyun, and C. -H. Kim, *J. Solid State Electrochem*. **8** (2004) 110.
[17]G. -J. Lee and S. -I. Pyun, *Electrochim. Acta* **51** (2006) 3029.
[18]P. L. Walker, Jr., F. Rusinko, Jr., and E. Raats, *J. Phys. Chem*. **59** (1955) 245.
[19]J. S. Mattson and H. B. Mark, Jr., *Activated Carbon: Surface Chemistry and Adsorption from Solution*, Marcel Dekker, New York, 1971.
[20]F. Caturla, M. Molina-Sabio, and F. Rodriguez-Reinso, *Carbon* **29** (1991) 999.
[21]F. Rodríguez-Reinoso and M. Molina-Sabio, *Carbon* **30** (1992) 1111.
[22]A. Ahmadpour and D.D. Do, *Carbon* **34** (1996) 471.
[23]C. Namasivayam and K. Kadirvelu, *Bioresource Technol*. **62** (1997) 123.
[24]S. R. Tennison, *Applied Catalysis A: General* **173** (1998) 289.
[25]C. -F. Chang, C.-Y. Chang, and W. -T. Tsai, *J. Colloid Interface Sci*. **232** (2000) 45.
[26]H. Teng and S. -C. Wang, *Carbon* **38** (2000) 817.
[27]Z. Ryu, J. Zheng, M. wang, and B. Zhang, *J. Colloid Interface Sci*. **230** (2000) 312.
[28]A. R. Sánchez, A. A. Elguézabal, and L. de La Torre-Saenz, *Carbon* **39** (2001) 1367.
[29]D. Lozanó-Castelló, M. A. Lillo-Ródenas, D. Cazorla-Amorós, and A. Linares-Solano, *Carbon* **39** (2001) 741.
[30]F. Suárez-García, J. I. Paredes, A. Martínez-Alonso, and Juan M.D. Tascón, *J. Mater. Chem*. **12** (2002) 3213.
[31]A. M. Puziy, O. I. Poddubnaya, A. Martínez-Alonso, and F. Suárez-García, J. M. D. Tascón, *Carbon* **41** (2003) 1181.
[32]K. Okada, N. Yamamoto, Y. Kameshima, and A. yasumori, *J. Colloid Interface Sci*. **262** (2003) 179.
[33]M. C. Baquero, L. Giraldo, J. C. Moreno, F. Suárez-García, A. Martínez-Alonso,

and J. M. D. Tascón, *J. Anal. Appl. Pyrolysis* **70** (2003) 779.
[34]J. A. Maciá-Agulló, B. C. Moore, D. Cazorla-Amorós and A. Linares-Solano, *Carbon* **42** (2004) 1367.
[35]F. -C. Wu, R. -L. Tseng, and R. -S. Juang, *J. Colloid Interface Sci*. **283** (2005) 49.
[36]E. Ruckenstein and Y. H. Hu, *Carbon* **36** (1998) 269.
[37]H. Tamon, H. Ishizaka, T. Araki, and M. Okazaki, *Carbon* **36** (1998) 1257.
[38]J.W. Lee, S.H. Yoon, T.H. Hyeon, S.M. Oh, and K.B. Kim, *Chem. Commun*. (1999) 2177.
[39]R. Ryoo, S. -H. Joo, and S. Jun, *J. Phys. Chem. B*, **103** (1999) 7743.
[40]S. J. Han and T. H. Hyeon, *Carbon* **37** (1999) 1645.
[41]D. Kawashima, T. Aihara, Y. Kobayashi, T. Kyotani, and A. Tomita, *Chem. Mater.* **12** (2000) 3397.
[42]S. J. Han, K. N. Sohn, and T. H. Hyeon, *Chem. Mater*. **12** (2000) 3337.
[43]J. W. Lee, K. N. Sohn, and T. H. Hyeon, *J. Am. Chem. Soc*. **123** (2001) 5146.
[44]S. H. Joo, S. J. Choi, I. Oh, J. Kwak, Z. Liu, O. Terasaki, and R. Ryoo, *Nature* **412** (2001) 169.
[45]Z. Li and M. Jaroniec, *Carbon* **39** (2001) 2077.
[46]Z. Li and M. Jaroniec, *J. Am. Chem. Soc*. **123** (2001) 9208.
[47]M. Kang, S. H. Yi, H. I. Lee, J. E. Yie, and J. M. Kim, *Chem. Commun*. (2002) 1944.
[48]W. W. Lukens and G. D. Stucky, *Chem. Mater*. **14** (2002) 1665.
[49]A. B. Fuertes and D. M. Nevskaia. *Micropor. Mesopor. Mater.* **62** (2003) 177.
[50]J. W. Lee, J. Y. Kim, and T. H. Hyeon, *Chem. Commun*. (2003) 1138.
[51]J. Yamashita, T. Ojima, M. Shioya, H. Hatori, and Y. Yamada, *Carbon* **41** (2003) 285.
[52]P. M. Barata-Rodrigues, T. J. Mays, and G. D. Moggridge, *Carbon* **41** (2003) 2231.
[53]Y. X. Wang, S. H. Tan, D. L. Jiang, and X. Y. Zhang, *Carbon* **41** (2003) 2065.
[54]S. -I. Pyun and C. -K. Rhee, *Electrochim. Acta* **49** (2004) 4171.
[55]G. -J. Lee and S. -I. Pyun, *Carbon* **43** (2005) 1804.
[56]P. Pfeifer and D. Avnir, *J. Chem. Phys*. **79** (1983) 3558.
[57]C. W. Lung and S. Z. Zhang, *Physica D* **38** (1989) 242.
[58]P. Pfeifer, Y. J. Wu, M. W. Cole, and J. Krim, *Phys. Rev. Lett.* **62** (1989) 1997.
[59]M. Jaroniec, *Fuel* **69** (1990) 1573.
[60]I. M. K. Ismail and P. Pfeifer, *Langmuir* **10** (1994) 1532.
[61]M. K. Wu, *Aerosol Sci. Technol.* **25** (1996) 392.
[62]R. Wojsz and A. P. Terzyk, *Comput. Chem.* **20(4)** (1996) 427.
[63]B. Sahouli, S. Blacher, and F. Brouers, *Langmuir* **13** (1997) 4391.
[64]M. Sato, T. Sukegawa, T. Suzuki, and K. Kaneco, *J. Phys. Chem. B* **101** (1997) 1845.
[65]P. Pfeifer and K. Y. Liu, *in Equilibria and Dynamics of Gas Adsorption on Heterogeneous Solid Surfaces,* Ed. by W. Rudziński, W.A. Steele, and G. Zgrablich, Elsevier, New York, 1997, p. 625.
[66]N. R. Khalili, M. Pan, and G. Sandí, *Carbon* **38** (2000) 573.
[67]C. Lin, J. A. Ritter, and B. N. Popov, *J. Electrochem. Soc.* **146** (1999) 3639.
[68]S. Shiraishi, H. Kurihara, L. Shi, T. Nakayama, and A. Oya, *J. Electrochem. Soc.* **149** (2002) A855.
[69]R. W. Pekala, C. T. Alviso, F. M. Kong, and S. S. Hulsey, *J. Non-Cryst. Solids* **145** (1992) 90.
[70]R. W. Pekala, J. C. Farmer, C. T. Alviso, T. D. Tran, S. T. Mayer, J. M. Miller, and B. Dunn, *J. Non-Cryst. Solids* **225** (1998) 74.

[71]R. Zhang, Y. Lu, L. Zhan, X. Liang, G. Wu, and L. Ling, *Carbon* **41** (2002) 1660.
[72]R. Zhang, W. Li, X. Liang, G. Wu, Y. Lü, L. Zhan, C. Lu, and L. Ling, *Micropor. Mesopor. Mater.* **62** (2003) 17.
[73]R. W. Pekala, *J. Mater. Sci.* **24** (1989) 3221.
[74]R. W. Pekala, C. T. Alviso, X. Lu, J. Gross, and J. Fricke, *J. Non-Cryst. Solids* **188** (1995) 34.
[75]X. Lu, R. Caps, J. Fricke, C.T. Alviso, and R. W. Pekala, *J. Non-Cryst. Solids* **188** (1995) 226.
[76]S. M. Manocha, D. Y. Vashistha, and L. M. Manocha, *J. Mater. Sci. Lett.* **16** (1997) 705.
[77]H. Müller, P. Rehak, C. Jäger, J. Hartmann, N. Meyer, and S. Spange, *Adv. Mat.* **12** (2000) 1671.
[78]S. Braunauer, L. S. Deming, W. E. Deming, and E. Teller, *J. Am. Chem. Soc.* **62** (1940) 1723.
[79]K. S. W. Sing, D.H. Everett, R. A. W. Haul, L. Moscou, R.A. Pierotti, J. Rouquérol, and T. Siemieniewska, *Pure Appl. Chem.* **57** (1985) 603.
[80]F. Stoeckli, T. A. Centeno, A. B. Fuertes, and J. Muňiz, *Carbon* **34** (1996) 1201.
[81]Z. Li, M. Kruk, M. Jaroniec, and S. -K. Ryu, *J Colloid Interface Sci*. **204** (1998) 151.
[82]Z. Ryu, J. Zheng, and M. Wang, *Carbon* **36** (1998) 427.
[83]M. El-Merraoui, M. Aoshima, and K. Kaneko, *Langmuir* **16** (2000) 4300.
[84]A. H. Lu and J. T. Zheng, *J Colloid Interface Sci*. **236** (2001) 369.
[85]M. Kruk and M. Jaroniec, *Chem. Mater*. **12** (2000) 222.
[86]M. Kruk and M. Jaroniec, *Chem. Mater.* **13** (2001) 3169.
[87]R. Ryoo, I. -S. Park, S. Jun, C. W. Lee, M. Kruk, and M. Jaroniec, *J. Am. Chem. Soc.* **123** (2001) 1650.
[88]Q. Huo, D. I. Margolese, and G. D. Stucky, *Chem. Mater*. **8** (1996) 1147.
[89]M. Kruk and M. Jaroniec, *Langmuir* **13** (1997) 6267.
[90]H. -P. Lin, S. -T. Wong, C. -Y. Mou, and C. -Y. Tang, *J. Phys. Chem. B* **104** (2000) 8967.
[91]P. J. Kooyman, M. J. Verhoef, and E. Prouzet, *Stud. Surf. Sci. Catal*. **129** (2000) 535.
[92]S. Brunauer, P. H. Emmett, and E. Teller, *J. Am. Chem. Soc*. **60** (1938) 309.
[93]I. Langmuir, *J. Am. Chem. Soc*. **40** (1918) 1631.
[94]P. A. Webb and C. Orr, *Analytical Methods in Fine Particle Technology*, Micrometritics Instrument Corporation, Norcross, 1997.
[95]M.M. Dubinin and L.V. Radushkevich, *Proc. Acad. Sci. USSR* **55** (1947) 331.
[96]M. Polanyi, *Verb. Deutsch. Phyrik. Ges.* **16** (1914) 1012.
[97]M. M. Dubinin and H. F. Stoeckli, *J. Colloid Interface Sci*. **75** (1980) 34.
[98]M. M. Dubinin and B. A. Astakhov, *Izv. AN. SSSR. Ser. Khim*. **5** (1971) 11.
[99]G. Horvath and K. Kawazoe, *J. Chem. Eng. Jpn.* **16** (1983) 470.
[100]D. H. Everett and J. C. Powl, *J. Chem. Soc., Faraday Trans.* **72** (1976) 619.
[101]A. Saito and H. C. Foley, *AIChE Journal* **37** (1991) 429.
[102]L. S. Cheng and R. T. Yang, *Chem. Eng. Sci.* **49** (1994) 2599.
[103]S. J. Gregg and K. S. W. Sing, *Adsorption, surface area and porosity*, Academic Press, New York, 1982.
[104]E. P. Barrett, L. G. Joyner, and P. P. Halenda, *J. Am. Chem. Soc*. **73** (1951) 373.
[105]B. B. Mandelbrot, *The Fractal Geometry of Nature*, W.H. Freeman and Company, New York, 1983.
[106]H. O. Peitgen and D. Saupe, Ed., *The Science of Fractal Images*, Springer Verlag, New York, 1988.

[107]C. A. Pickover, *Computers, Pattern, Chaos and Beauty*, St. Martin's Press, New York, 1990.
[108]H. O. Peitgen, H. Jürgens, and D. Saupe, *Fractals for the Classroom: Introduction to Fractals and Chaos*, Springer Verlag, New York, 1992.
[109]R. N. Mantegna and H. E. Stanley, *Nature* **376** (1995) 46.
[110]M. H. R. Stanley, L. A. N. Amaral, S.V. Buldyrev, S. Havlin, H. Leschhorn, P. Maass, M. A. Salinger, and H. E. Stanley, *Nature* **379** (1996) 804.
[111]H. Takayasu and K. Okuyama, *Fractals* **6** (1998) 67.
[112]H. Takayasu, M. Takayasu, M.P. Okazaki, K. Marumo, and T. Shimizu, in *Paradigms of Complexity*, Ed. by M.M. Novak, World Scientific, 2000, p. 243.
[113]T. Lours, J. Zarzycki, A. Craievich, D. I. dos Santos, and M. Aegerter, *J. Non-Cryst. Solids* **95** (1987) 1151.
[114]W. I. Friesen and R. J. Mikula, *J Colloid Interface Sci.* **120(1)** (1987) 263.
[115]J. J. Friel and C. S. Pande, *J. Mater. Res.* **8(1)** (1993) 100.
[116]P. Tang, N. Y. K. Chew, H. K. Chan, and J.A. Raper, *Langmuir* **19** (2003) 2632.
[117]D. Avnir and D. Farin, *J. Chem. Phys*. **79** (1983) 3566.
[118]P. Pfeifer, D. Avnir, and D. Farin, *Surf. Sci.* **126** (1983) 569.
[119]D. Avnir, D. Farin, and P. Pfeifer, *Nature* **308** (1984) 261.
[120]D. Avnir, D. Farin, and P. Pfeifer, *J. Colloid Interface Sci.* **103** (1985) 112.
[121]D. Farin, S. Pelog, D. Yavin, and D. Avnir, *Langmuir* **1** (1985) 399.
[122]A. Y. Myer, D. Farin, and D. Avnir, *J. Am. Chem. Soc.* **108** (1986) 7897.
[123]D. Avnir, *J. Am. Chem. Soc.* **109** (1987) 2931.
[124]D. Farin and D. Avnir, *J. Phys. Chem.* **91** (1987) 5517.
[125]D. Farin and D. Avnir, *J. Am. Chem. Soc.* **110** (1988) 2039.
[126]A. V. Neimark, *Adsorpt. Sci. Technol.* **7** (1990) 210.
[127]D. K. Ludlow and T. P. Moberg, *Anal. Instrum.* **19** (1990) 113.
[128]K. Kaneko, *Langmuir* **7** (1991) 109.
[129]M. Sato, T. Sukegawa, T. Suzuki, S. Hagiwara, and K. Kaneko, *Chem. Phys. Lett.* **181** (1991) 526.
[130]T. Suzuki and T. Yano, *Biol. Chem.* **55** (1991) 967.
[131]D. Avnir, D. Farin, and P. Pfeifer, *New J. Chem.* **16** (1992) 439.
[132]Y. Lefebvre, S. Lacelle, and C. Jolicoeur, *J. Mater. Res.* **7** (1992) 1888.
[133]W. C. Conner and C. O. Bennett, *J. Chem. Soc., Faraday Trans.* **89** (1993) 4109.
[134]R. F. Cracknell, P. Gordon, and K. E. Gubbins, *J. Phys. Chem.* **97** (1993) 494.
[135]K. Kaneko, R. F. Cracknell, and D. Nichlson, *Langmuir* **10** (1994) 4606.
[136]T. Suzuki, K. Kaneko, N. Setoyama, M. Maddox, and K. E. Gubbins, *Carbon* **34** (1996) 909.
[137]P. Pfeifer and M. W. Cole, *New J. Chem.* **14** (1990) 221.
[138]P. Pfeifer, J. Kenntner, and M. W. Cole, in *Fundamentals of Adsorption*, Ed. by A. B. Mersmann and S. E. Scholl, American Institute of Chemical Engineers, New York, 1991, p. 689.
[139]J. Frenkel, *Kinetic Theory of Liquids*, Clarendon, Oxford, 1946.
[140]G. D. Halsey, *J. Chem. Phys.* **16** (1948) 931.
[141]T. L. Hill, *Adv. Catal.* **4** (1952) 211.
[142]S. -B. Lee, S. -I. Pyun, and C. -K. Rhee, *Carbon* **41** (2003) 2446.
[143]A. P. Terzyk, R. Wojsz, G. Rychlicki, and P. A. Gauden, *Colloids and Surfaces A: Physicochemical and Engineering Aspects* **119** (1996) 175.
[144]R. Wojsz and A. P. Terzyk, *Comput. Chem.* **21(2)** (1997) 83.
[145]A. P. Terzyk, P. A. Gauden, G. Rychlicki, and R. Wojsz, *Colloids Surf. A: Physicochemical and Engineering Aspects* **136** (1998) 245.
[146]A. P. Terzyk, P. A. Gauden, G. Rychlicki, and R. Wojsz, *Colloids Surf.* **152** (1999) 293.

[147]P. A. Gauden, A. P. Terzyk, and G. Rychlicki, *Carbon* **39** (2001) 267.
[148]P. A. Gauden, A. P. Terzyk, G. Rychlicki, and P. Kowalczyk, *J. Colloid Interface Sci.* **244** (2001) 439.
[149]A. P. Terzyk and P.A. Gauden, *The Arabian Journal for Science and Engineering* **28** (2003) 133.
[150]M. M. Dubinin, *J. Colloid Interface Sci.* **23** (1967) 487.
[151]M. Endo, K. Takeuchi, Y. Sasuda, K. Matsubayashi, K. Oshida, and M. S. Dresselhaus, *Electron. Commun. Jpn.* **77** (1994) 139.
[152]K. Oshida, K. Kogiso, K. Matsubayashi, K. Takeuchi, S. Kobayashi, M. Endo, M.S. Dresselhaus, and G. Dresselhaus, *J. Mater. Res*. **10** (1995) 2507.
[153]M. Endo, T. Furuta, F. Minoura, and C. Kim, K. Oshida, G. Dresselhaus, and M.S. Dresselhaus, *Supermolecular Science* **5** (1998) 261.
[154]B. B. Mandelbrot, *Phys. Scr.* **32** (1985) 257.
[155]J. Feder, *Fractals*, Plenum Press, New York, 1988.
[156]J. M. Gómez-Rodríguez, A. M. Baró, and R. C. Salvarezza, *J. Vac. Sci. Technol. B* **9** (1991) 495.
[157]P. Ocon, P. Herrasti, L. Vázquez, R. C. Salvarezza, J. M. Vara, and A. J. Arvia, *J. Electroanal. Chem.* **319** (1991) 101.
[158]J. M. Gómez-Rodríguez, A. M. Baró, L. Vázquez, R. C. Salvarezza, J. M. Vara, and A. J. Arvia, *J. Phys. Chem.* **96** (1992) 347.
[159]P. Herrasti, P. Ocón, R.C. Salvarezza, J. M. Vara, L. Viázquez, and A. J. Arvia, *Electrochim. Acta* **37** (1992) 2209.
[160]R. de Levie, *Electrochim. Acta* **9** (1964) 1231.
[161]R. de Levie, *Electrochim. Acta* **10** (1965) 113.
[162]R. de Levie, *Advances in Electrochemistry and Electrochemical Engineering*, Ed. by P. Delahay, Vol. VI, John Wiley & Sons, New York, 1967, p. 329.
[163]W. Scheider, *J. Phys. Chem.* **79** (1975) 127.
[164]H. Keiser, K. D. Beccu, and M. A. Gutjahr, *Electrochim. Acta* 21 (1976) 539.
[165]M. Kramer and M. Tomkiewicz, *J. Electrochem. Soc.* **131** (1984) 1283.
[166]Nyikos and T. Pajkossy, *Electrochim. Acta* **30** (1985) 1533.
[167]T. Pajkossy, *J. Electroanal. Chem*. **364** (1994) 111.
[168]K. Eloot, F. Debuyck, M. Moors, and A. P. Van Peteghem, *J. Appl. Electrochem*. **25** (1995) 326.
[169]K. Eloot, F. Debuyck, M. Moors, and A. P. Van Peteghem, *J. Appl. Electrochem*. **25** (1995) 334.
[170]T. Momma, X. Liu, T. Osaka, Y. Ushio, and Y. Sawada, *J. Power Sources* **60** (1996) 249.
[171]Z. Kerner and T. Pajkossy, *J. Electroanal. Chem*. **448** (1998) 139.
[172]H. -K. Song, Y. -H. Lee, and Le H. Dao, *Electrochim. Acta* **44** (1999) 3513.
[173]H. -K. Song, H. -Y. Hwang, K. -H. Lee, and Le H. Dao, *Electrochim. Acta* **45** (2000) 2241.
[174]J. Bisquert, *Phys. Chem. Chem. Phys*. **2** (2000) 4185.
[175]J. Bisquert, G. Garcia-Belmonte, F. Fabregat-Santiago, N. S. Ferriols, P. Bogdanoff, and E. C. Pereira *J. Phys. Chem. B* **104** (2000) 2287.
[176]Z. Kerner and T. Pajkossy, *Electrochim. Acta* **46** (2000) 207.
[177]D. Qu, *J. Power Sources* **109** (2002) 403.
[178]C. -H. Kim, S. -I. Pyun, and J. -H. Kim, *Electrochim. Acta* **48** (2003) 3455.
[179]A. Le Mehaute and G. Crepy, *Solid State Ionics* **9&10** (1983) 17.
[180]A. Le Mehaute, *J. Stat. Phys.* **36** (1984) 665.
[181]S. H. Liu, *Phys. Rev. Lett.*, **55** (1985) 529.
[182]B. Sapoval, *Solid State Ionics* **23** (1987) 253.
[183]T. C. Halsey, *Phys. Rev. A* **35** (1987) 3512.

[184]T. Kaplan, L. J. Gray, and S.H. Liu, *Phys. Rev. B* **35** (1987) 5379.
[185]J. C. Wang, *Electrochim. Acta* **33** (1988) 707.
[186]R. M. Hill and L. A. Dissado, *Solid State Ionics* **26** (1988) 295.
[187]W. H. Mulder and J. H. Sluyters, *Electrochim. Acta* **33** (1988) 303.
[188]Y. T. Chu, *Solid State Ionics* **26** (1988) 299.
[189]M. Blunt, *J. Phys. A: Math. Gen.* **22** (1989) 1179.
[190]A. Maritan and F. Toigo, *Electrochim. Acta* **35** (1990) 141.
[191]T. Pajkossy and L. Nyikos, *Phys. Rev. B* **42** (1990) 709.
[192]M. A. Daley, D. Tandon, J. Economy, and E. J. Hippo, *Carbon* **34** (1996) 1191.
[193]J. P. Randin and E. Yeager, *J. Electroanal. Chem. and Interfacial Electrochem*. **36** (1972) 257.
[194]J. P. Randin and E. Yeager, *J. Electroanal. Chem. and Interfacial Electrochem*. **58** (1975) 313.
[195]A. J. Groszek, *Carbon* **25** (1987) 717.
[196]K. Kinoshita, *Carbon: Electrochemical and Physicochemical Properties*, John Wiley & Sons, New York, 1988, p. 293.
[197]H. Marsh, E. A. Heintz, and F. R. Reinoso, *Introduction to Carbon Technologies*, Universidad de Alicante, Secretariado de Publicaciones, 1997, p. 36
[198]H. Marsh and F. R. Reinoso, *Sciences of Carbon Materials*, Universidad de Alicante, Secretariado de Publicaciones, 2000, p. 8.
[199]A. Sadkowski, *Electrochim. Acta* **38** (1993) 2051.
[200]C.P. Smith and H.S. White, *Langmuir* **9** (1993) 1.
[201]M.G. Sullivan, B. Schnyder, M. Bärtsch, D. Alliata, C. Barbero, R. Imhof, and R. Kötz, *J. Electrochem. Soc*. **147** (2000) 2636.
[202]M.G. Sullivan, R. Kötz, and O. Haas, *J. Electrochem. Soc.* **147** (2000) 308.
[203]C. -T. Hsieh and H. Teng, *Carbon*, **40** (2002) 667.
[204]K. Kinoshita and J. A. S. Bett, *Carbon*, **13** (1975) 405.
[205]K. Kinoshita and X. Chu, "Carbon for Supercapacitors"; in *Proceedings of the Symposium on Electrochemical Capacitors*, F. M. Denlick and M. Tomkiewicz, Editors, PV 95-29, The Electrochemical Society Proceeding Series, Pennington, NJ, 1995, p. 171-180.



http://www.springer.com/978-0-387-46107-6

Modern Aspects of Electrochemistry 41
Vayenas, C.G. (Ed.)
2007, XI, 308 p., Hardcover
ISBN: 978-0-387-46107-6